https://doi.org/10.5194/essd-2026-352
Preprint. Discussion started: 11 September 2026

Open Access Earth System Science Data Discussions

A convective-scale reanalysis for the ‘Swabian MOSES 2023’ field campaign

Julia Thomas[1], Hendrik Reich[2], Thorsten Steinert[2], Gernot Geppert[2], Klaus Stephan[2], Anselm Erdmann[1], Philipp Gasch[1], Maxime Hervo[3], Jan Keller[2], Alberto Carrassi[4], Peter Knippertz[1], and Annika Oertel[1]

[1]Karlsruhe Institute of Technology, Institute of Meteorology and Climate Research Troposphere Research, Karlsruhe, Germany
[2]Deutscher Wetterdienst, Offenbach, Germany
[3]Federal Office of Meteorology and Climatology MeteoSwiss, Payerne, Switzerland
[4]University of Bologna, Department of Physics and Astronomy, Bologna, Italy

Correspondence: Julia Thomas (julia.thomas@kit.edu)

Abstract. A reanalysis can be considered the most complete representation of the atmospheric state given all available observations as well as the model background. Via data assimilation, a reanalysis allows assessing the non-local influence of observations on the time evolution of the modeled state, while aiming to maintain the physical consistency of the model state. Here, we present the pioneering, 3-month convective-scale campaign reanalysis of the ‘Swabian MOSES 2023’ campaign, consisting of a control (CTRL) dataset without and a campaign (CMPG) dataset with additional field campaign observations from the mobile atmospheric measurement platform KITcube during June, July and August 2023. Both are computed at hourly resolution on a 2.2 km grid centered over Germany with the quasi-operational data assimilation framework by Deutscher Wetterdienst which is based on a Local Ensemble Transform Kalman Filter. CMPG incorporates additional ground-based remote-sensing and in situ observations from the southwest German mountain ranges of the Black Forest and Swabian Jura, a region with moderately complex terrain. The unprecedentedly dense network of 12 Doppler wind lidars, one X-band precipitation radar, two additional radiosounding sites, Global Navigation Satellite Systems receivers, and meteorological masts increases the number of observations in the approximately 10^5 km^2 campaign area by 45 % compared to the operational measurement network. As expected, the assimilation reduces the difference between observations and model fields. Specifically, the standard deviation of the observation-to-model difference across all additional observations is reduced by 10% to 35% after assimilation. Updates of the model background are predominantly introduced in the lower troposphere and in the campaign region itself, but differences between CMPG and CTRL extend all over Germany, eastern France, and northern Italy. Mean absolute differences in the campaign region reach up to the order of $1.5\,\mathrm{m\,s^{-1}}$ in wind speed, 0.4 K in temperature, and $0.7\,\mathrm{g\,kg^{-1}}$ in humidity. This pioneering campaign reanalysis can be employed to quantify the influence of individual observations and different observation types and to diagnose potential model deficiencies in complex terrain. It further serves as a high-resolution reference for detailed case studies targeting high-impact weather and provides a basis for re-forecast experiments to quantify observation impact on forecasts.

https://doi.org/10.5194/essd-2026-352
Preprint. Discussion started: 11 September 2026

1 Introduction

Forecasting mesoscale events, such as convective storms, remains one of the largest challenges of numerical weather prediction (NWP), even for state-of-the-art, convection-permitting, ensemble systems (Hohenegger and Schär, 2007; Baldauf et al., 2011; Clark et al., 2016). In addition to improving the forecasting system itself, by for example improving its parametrization schemes (Keane et al., 2014; Kober and Craig, 2016; Goger et al., 2016; Sakradzija et al., 2016; Hirt et al., 2019; Grundner et al., 2022), increasing the grid resolution (e.g., Goger and Dipankar, 2024) and the number of ensemble members (e.g., Richardson, 2000; Raynaud and Bouttier, 2017; Leutbecher, 2019), an accurate representation of the atmospheric state at forecast initialization is crucial for a skillful forecast (Navon, 2009; Yano et al., 2018; Carrassi et al., 2018; Gustafsson et al., 2018). The intrinsic predictability for convective events is low, with a forecast horizon of less than a day (Hohenegger and Schär, 2007; Durran and Weyn, 2016). Therefore, as the model resolution increases and becomes able to resolve such processes, ensemble data assimilation (Houtekamer and Zhang, 2016) at high spatial and temporal resolution becomes important. For example, a localized version of the ensemble transform Kalman filter (LETKF; Hunt et al., 2007) presents a suitable method for convective-scale data assimilation in convection permitting models. The LETKF has been used operationally for the high-resolution regional system of Deutscher Wetterdienst since 2017 (Bishop et al., 2001; Schraff et al., 2017) and its introduction has led to significant improvements of the forecast skill.

Observing the atmospheric boundary layer: current status and limitations

Mesoscale low-level convergence and moisture fields are key for the initiation and development of convective systems (e.g., Wilson and Schreiber, 1986; Weckwerth et al., 2014; Marquis et al., 2021). Therefore, an accurate representation of the state of the atmospheric boundary layer (ABL) is crucial for forecasting the initiation and development of convective systems (Weyn and Durran, 2017; Parsons et al., 2019; Schumacher and Rasmussen, 2020). Moreover, the ABL is characterized by high temporal variability and strong gradients, especially above complex terrain. Thus, observations are needed at sufficiently high temporal and spatial resolution to represent this spatiotemporal variability. While more and more observations from satellites are being assimilated (not only in global but also in regional models (Schomburg et al., 2015; Scheck et al., 2020)), the number of observations in the ABL has not increased commensurately with the increasing model resolution, and the ABL remains one of the undersampled parts of the atmosphere (Baker et al., 2014; Geerts et al., 2018; Bell et al., 2020; Team et al., 2021). Radiosoundings provide high-resolution in situ observations of the most important atmospheric variables, including wind, temperature and humidity. However, they are typically only launched twice a day and at few locations. Similarly, vertical profiles obtained from commercial aircraft during ascent and descent (i.e., around airports) are distributed inhomogeneously in space and are available mostly during daytime (De Haan, 2011). Precipitation radars provide measurements with high spatial and temporal resolution, but only for rainy and not clear air conditions. Near-surface measurements from $2\,\mathrm{m}$- or $10\,\mathrm{m}$-masts cannot profile the ABL, and satellite radiances typically provide information from higher up in the atmosphere. Therefore, current operationally assimilated observation systems do not provide a satisfactory representation of the spatiotemporal atmospheric state, especially within the ABL. Thus, although the triggering mechanisms are – to some extent – understood, forecasting

https://doi.org/10.5194/essd-2026-352
Preprint. Discussion started: 11 September 2026

convective storms remains a challenge. At the same time, convective storms are one of the dominant natural threats in Central Europe (Hoeppe, 2016; Taszarek et al., 2019) and their number and intensity is expected to increase in Central Europe, especially near mountain ranges (Raupach et al., 2021; Feldmann et al., 2025; Mohr et al., 2026), emphasizing the need to improve forecast quality. Previous studies have shown that assimilating high-resolution, ground-based, remote-sensing observations of the ABL can improve the model representation and can have a positive impact on short-range forecasts (Kawabata et al., 2014; Caumont et al., 2016; Coniglio et al., 2019; Bachmann et al., 2020; Hristova-Veleva et al., 2021; Nomokonova et al., 2023; Zeng et al., 2024; Vural et al., 2024; Thomas et al., 2025). To date, no widespread and dense network of ABL profiling instruments exists in Europe (Cimini et al., 2020).

Challenges for convective-scale data assimilation in complex terrain

Modeling mesoscale atmospheric processes in mountainous areas can be more challenging than over flat terrain, as physical parameterizations are typically developed for horizontally homogeneous and flat terrain (Serafin et al., 2018). Moreover, steep slopes, non-homogeneous surface roughness and high spatial variability of the terrain itself are still coarsely resolved in kilometer-scale models. Wind profilers in mountainous environments cannot sample the spatial heterogeneity of the flow and their observations may be non-representative due to local effects (Hacker et al., 2018). For example, a wind profile retrieved from an instrument installed in a narrow mountain valley cannot represent the wind conditions at the mountain top or in the neighboring valley, although these locations may be less than a few gridpoints apart and lie well within the observation's localization radius. Together, this exacerbates representativity errors, which impede incorporating information from observations into the model via data assimilation (Janjić et al., 2018). A recent study by Bugnard et al. (2025) has shown that even a $1\,\mathrm{km}$ resolution analysis overestimates nighttime ground temperature in a $1.5\,\mathrm{km}$ wide Swiss valley because of missed temperature inversions and cannot represent the hourly variability of Doppler lidar retrieved wind profiles, although monthly medians match the observations well. Therefore, improving the model analysis in the mountain boundary layer requires kilometer to sub-kilometer scale model resolution. Additionally, observational systems able to resolve the high spatiotemporal variability of humidity, temperature, and wind in the lower troposphere above complex terrain are needed. Increasing the number of operationally deployed instruments is an expensive and long-term process. To enable short-term improvements and data assimilation experiments, observational field campaigns, albeit limited in time and area covered, can provide a wealth of data at high temporal resolution. Field campaign observations can serve to (i) test and monitor the applicability of assimilating novel observation types, (ii) characterize their influence on the analysis and, (iii) assess their impact on the forecast. Moreover, using campaign observations of the lower-troposphere to create and improve convective-scale analyses offers a large potential for (iv) understanding mesoscale processes, (v) studying model deficiencies and, (vi) assessing the predictability of mesoscale weather events. Unlike model verification, which is limited to a comparison at the observation locations, data assimilation opens the possibility of assessing the non-local influence of additional observations spatially and temporally distant from the observation location.

https://doi.org/10.5194/essd-2026-352
Preprint. Discussion started: 11 September 2026

Data assimilation methods commonly used in atmospheric prediction

Data assimilation aims at identifying the most likely atmospheric state considering both the information provided by the model and the information provided by the observations. Methods commonly used for data assimilation in atmospheric science range from comparatively simple relaxation approaches to fully flow-dependent statistical estimation methods (Carrassi et al., 2018). Nudging (Stauffer and Seaman, 1990) continuously relaxes the model state towards observations and is computationally inexpensive, but it cannot consistently spread observational information in space and between variables. Variational methods such as three-dimensional variational assimilation (3D-Var; Lorenc, 1986; Courtier et al., 1998) and four-dimensional variational assimilation (4D-Var; Le Dimet and Talagrand, 1986; Bonavita and Lean, 2021) provide a best estimate of the modeled state of the atmosphere by minimizing a cost function that balances observations and prior model information given their respective error covariances. 4D-Var additionally accounts for the temporal evolution of the atmospheric state within a defined assimilation window. These methods are well established, but their often climatological background-error statistics are not flow dependent. Moreover, 4D-Var is computationally demanding, especially at convection-permitting resolution, and therefore – to date – not commonly applied for kilometer-scale operational NWP systems. Nowadays, hybrid variational-ensemble methods are the operational frontier and are developed or already in use at many operational weather services such as ECMWF (ECMWF, 2021), Meteo France (Chambon et al., 2023; Brousseau et al., 2025), the Canadian Weather Service (Buehner et al., 2025), Deutscher Wetterdienst (Müller et al., 2025) and UK Met Office (Clayton et al., 2013). Hybrid data assimilation methods merge variational and ensemble approaches in order to mitigate their reciprocal limitations and to strengthen their advantages. They rely on the nonlinear optimization nature of the variational methods and use the flow-dependent ensemble to solve the optimization problem in several ways, leading to various formulations of the hybridization. Ensemble Kalman filter methods estimate background-error covariances from an ensemble of short-range forecasts and therefore adapt the background error covariances naturally to the current flow situation (Evensen, 1994; Houtekamer and Mitchell, 1998). The LETKF presents a computationally efficient, local implementation of the ensemble Kalman Filter. Its flow-dependent and spatially localized covariance structure makes it particularly suitable for high-resolution applications in complex terrain, where the temporal and spatial variability of the atmospheric state is typically larger than over flat terrain. It is operationally applied in regional data assimilation systems for example by Deutscher Wetterdienst (Schraff et al., 2016), MeteoSwiss (Lapillonne et al., 2026) and the Italian Meteorological Service (Bonavita et al., 2008).

Campaign-based reanalyses

A number of reanalyses based on observational campaigns have been performed in the past, e.g. for the Fronts and Atlantic Storm-Track Experiment (FASTEX; Desroziers et al., 2003), for the Mesoscale Alpine Programme (MAP; Keil and Cardinali, 2004), several for short periods of the Mesoscale Predictability Experiment (MPEX; Weisman et al., 2015), and for the first special observation period of the Hydrological cycle in the Mediterranean Experiment (HyMeX; Fourrié et al., 2019). Desroziers et al. (2003) assimilated additional ship and buoy observations as well as dropsonde profiles released from FASTEX aircraft and additional radiosoundings launched from land-based upper-air stations, by the four FASTEX ships or by

https://doi.org/10.5194/essd-2026-352
Preprint. Discussion started: 11 September 2026

Open Access Earth System Science Data Discussions

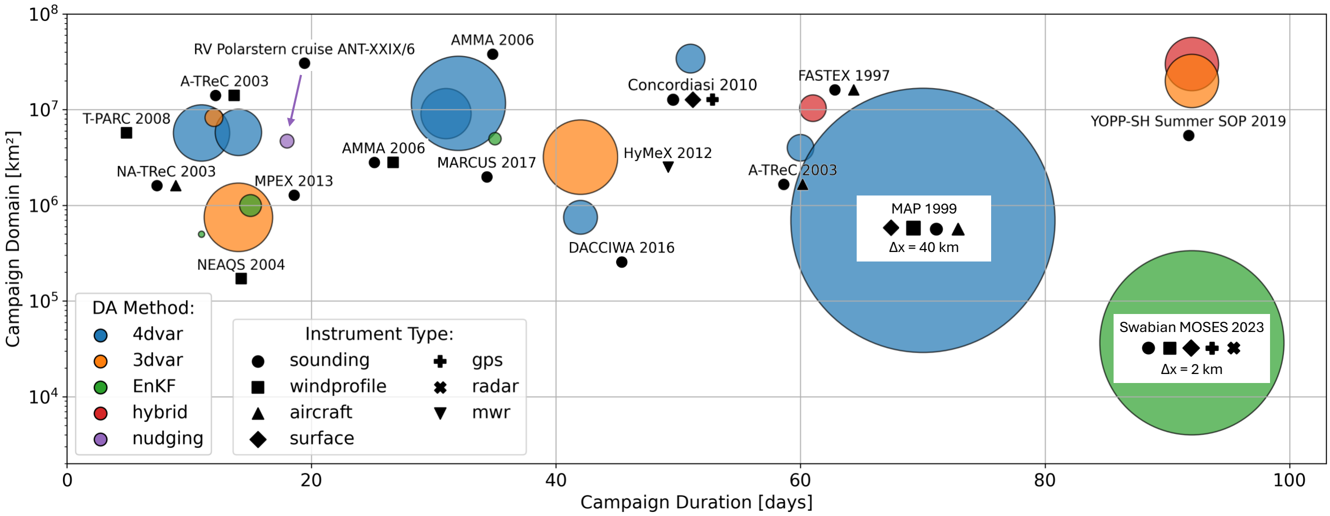

Figure 1. Overview of selected data assimilation studies based on atmospheric field campaigns sorted by duration and spatial extent (please note the logarithmic scale). The size of the colored circles scales with the number of assimilated atmospheric profile observations, e.g. as obtained from soundings and wind profilers. The symbols represent the type of assimilated campaign observations, and the colors indicate the applied data assimilation method (blue: 4D-Var; orange: 3D-Var; green: EnKF; red: hybrid; purple: nudging). Name and year of the respective campaign are given as labels. Δx refers to the grid spacing of the reanalysis.

Automated Shipboard Aerological Programme (ASAP) ships. They found a vertically homogeneous $30\,\%$ reduction in root mean square analysis departures and a $10\,\%$ reduction in root mean square background departures between the campaign and the control assimilation experiment. The positive impact was still present in $12\,$h-, $24\,$h-, and $36\,$h-forecasts evaluated downstream of the main field campaign area. Keil and Cardinali (2004) created a comprehensive reanalysis of the MAP Special Observing Period lasting 70 days from September to November 1999. They assimilated 55,000 additional atmospheric profiles, mostly from 16 wind profilers, and soundings from extra radiosonde and dropsonde launches across the Alpine domain and neighboring parts of France, Italy, and Germany, creating one of the largest campaign reanalyses at approximately $40\,$km grid spacing using 4D-Var. The assimilation of additional MAP observations resulted in a weakening of the cyclonic flow over central Europe and of the mid-tropospheric westerly wind over the Alpine region and led to moister conditions in the southern Alpine region, southern France and over the Adriatic Sea. However, a comparison with independent GPS measurements revealed that the reanalysis was slightly too dry. The MPEX experiment (Weisman et al., 2015) was designed to test the hypothesis that enhanced observations over the Rocky Mountains region can improve the forecast of convective initiation and the evolution of thunderstorms downstream over the high plains. Different studies (Hitchcock et al., 2016; Romine et al., 2016; Coniglio et al., 2016) assimilated different subsets of the additional campaign soundings in order to improve the prediction of convective events. They consistently found that assimilating additional sounding profiles is beneficial, however, only when the observations sample key features of the pre-convective environment and are placed appropriately relative to initiation, support-

https://doi.org/10.5194/essd-2026-352
Preprint. Discussion started: 11 September 2026

Open Access Earth System Science Data Discussions

ing the idea of targeted observations. The second HyMeX reanalysis created by Fourrié et al. (2019) revealed improvements in the $48\,\mathrm{h}$ forecast range for temperature, relative humidity and wind. However, they compare the second HyMeX reanalysis, computed with an improved model version and background error matrix tailored to the campaign period to real-time forecasts from years earlier. Therefore, improvements in their study are not solely attributable to data assimilation effects.

A new reanalysis dataset based on the Swabian MOSES 2023 campaign

In this study, we present two reanalyses: a 3-months campaign reanalysis dataset utilizing observations from the Swabian MOSES 2023 campaign (Handwerker et al., 2025) in addition to operationally available observations and a control reanalysis dataset built with the same setup but without assimilating additional campaign observations. Specifically, the campaign reanalysis includes the assimilation of in situ and remote sensing instrumentation from KITcube (Kalthoff et al., 2013), KIT's mobile atmospheric measurement platform deployed during the campaign, and additional observations by MeteoSwiss in addition to all operationally available observations. Figure 1 illustrates how the Swabian MOSES 2023 campaign reanalysis fits in the ecosystem of previous reanalyses, its main differences and similarities. In Fig. 1, we only consider studies that use multiple days of campaign observations and are dedicated to the campaign itself. In contrast, most data assimilation studies use data from a single research flight, ship excursion or from a newly installed instrument at a research site. Such studies are not considered. Since there is no sharp boundary between the 'individual' data impact studies and the 'complete' campaign reanalyses, Fig. 1 must not be considered an exhaustive list of all data assimilation studies. The majority of the campaign reanalyses shown in Fig. 1 rely on additional radiosounding observations (black circles in Fig. 1) and use a variational data assimilation system (predominantly 4D-Var; blue and orange circles in Fig. 1). Most of them are computed for periods of less than one month and assimilate data measured across a large area. The most comprehensive one is the MAP reanalysis Keil and Cardinali (2004). However, although this reanalysis employed one of the most advanced 4D-Var systems at that time, the spatial resolution of $40\,\mathrm{km}$ is far from resolving convective-scale features. Aiming for a higher resolution campaign reanalysis, 4D-Var is neither suitable for the temporal resolution needed (1-hour assimilation time step or less) nor is it affordable to run at high spatial resolution. Moreover, the 4D-Var background error covariance matrix is typically not flow-dependent and can thus not adequately represent the variability of the flow that is needed to quantify the uncertainty of the model state. To the best of our knowledge, no campaign reanalysis at kilometer-scale resolution has been built for multiple months, with multiple additional observation types, employing an ensemble Kalman filter for data assimilation.

This article is structured as follows: Section 2 describes the data assimilation system and the quasi-operational setup used to build the two reanalysis datasets. Section 3 briefly introduces the field campaign and describes the campaign observations used for assimilation in addition to the operationally assimilated observations. Section 4 characterizes the campaign reanalysis in observation space and Section 5 compares the campaign and the control reanalysis datasets in model space. Section 6 summarizes the main characteristics of the Swabian MOSES 2023 reanalysis and discusses its potential applications, its shortcomings, and future research applications to exploit this dataset.

https://doi.org/10.5194/essd-2026-352
Preprint. Discussion started: 11 September 2026

2 Data assimilation system and experimental setup

Table 1. Data assimilation setup for the 3-month campaign and the control reanalyses closely following the operational setup at Deutscher Wetterdienst.

Forecast model: ICON (Zängl et al., 2015)	
ICON model version	icon-2024.01-dwd-1.1
prognostic variables	air density, edge-normal velocity, vertical velocity, density potential temperature, water vapor mixing ratio, hydrometeor mixing ratios (cloud water, rain water, cloud ice, snow, graupel)
horizontal grid: - number of horizontal grid points - approximate grid spacing	icosahedral 542040 2.2 km
vertical coordinates	SLEVE (65 levels; Leuenberger et al. (2010))
lateral Boundary Conditions	from 3-hourly ICON-EU assimilation cycle with 1h-output (6.5 km (deterministic); 13 km (ensemble))
parameterizations: - convection: - microphysics - turbulence - radiation	 shallow convection only (Tiedtke (1989) and Bechtold et al. (2001)) one-moment cloud microphysics (Lin et al. (1983)) Raschendorfer (2001) ecRad (Hogan and Bozzo, 2018)
Data assimilation: KENDA (Schraff et al., 2016)	
assimilation method	LETKF Hunt et al. (2007)
output variables	pressure, temperature, meridional wind, zonal wind, mixing ratios of water vapor, snow, and ice, soil properties
cycling	continuous from 01 June 2023 to 31 August 2023
assimilation window	1 hour
ensemble members	40 members + 1 deterministic member
lateral Boundary Conditions	ICON-EU
additional settings - radar data assimilation - localization - ensemble inflation methods	 latent heat nudging (Stephan et al., 2008), EMVORADO (Zeng et al., 2016) adaptive; $r_{\mathrm{loc}}^{\mathrm{min}} = 50\,\mathrm{km}$, $r_{\mathrm{loc}}^{\mathrm{max}} = 100\,\mathrm{km}$ additive (Zeng et al., 2018), adaptive multiplicative (Anderson and Anderson, 1999), and relaxation to prior perturbations (Zhang et al., 2004)

The Swabian MOSES 2023 campaign reanalysis consists of two main parts: 1) The control reanalysis, **CTRL**, uses all operationally available observations in the period June–August (JJA) 2023 and 2) the campaign reanalysis, **CMPG**, includes all operationally available observations plus the campaign observations presented in Section 3. The setup for both experiments

https://doi.org/10.5194/essd-2026-352
Preprint. Discussion started: 11 September 2026

is quasi-operational, i.e. it follows the operational setup of Deutscher Wetterdienst as closely as possible. To avoid confusion, we distinguish the subset of operationally available observations by calling them **OP** from the additional campaign observations abbreviated by **SWM**, which refers to the name of the campaign. That way, CTRL includes only OP observations and CMPG includes OP + SWM observations and can be considered the most complete reanalysis currently available for summer 2023 in southern Germany. Both experiments are initialized with the operational analysis ensemble valid on 01 June 2023, 00 UTC and cycled continuously until 31 August 2023. The following subsections describe various aspects of the Kilometre-scale Ensemble Data Assimilation system (KENDA; Schraff et al., 2016) that is used to create our quasi-operational reanalyses. A summary of the setup is given in Table 1.

2.1 General approach

A full ensemble data assimilation cycle requires two main steps. First, in the forecast step (see Sect. 2.2), each member i of a background ensemble is obtained by integrating the i-th analysis ensemble member $\mathbf{x}_{\mathrm{t}_j}^{\mathrm{a}(i)}$, valid at time t_j, forward in time: $\mathbf{x}_{\mathrm{t}_{j+1}}^{\mathrm{b}(i)} = F_{j;j+1}\left(\mathbf{x}_{\mathrm{t}_j}^{\mathrm{a}(i)}\right)$. Second, at the analysis time step, the background ensemble is processed, together with all observations available within the assimilation interval, by the ensemble data assimilation system to get the updated analysis ensemble $\mathbf{x}_{\mathrm{t}_{j+1}}^{\mathrm{a}(i)}$ (see Sect. 2.3). The forecast and analysis steps then alternate sequentially in time.

2.2 The forecast step

The forward integration to produce the background ensembles is done using the Icosahedral Non-Hydrostatic Model (ICON) version *icon-2024.01-dwd-1.1* on a regional domain covering Germany and its neighboring countries (ICON-D2; see Fig. 2a). The assimilation time step is one hour, i.e. $\mathrm{t}_{j+1} - \mathrm{t}_j = 1\,\mathrm{h}$. The grid is an icosahedral R19B08 grid with 542,040 cells per layer and 65 vertical layers, which corresponds to an effective horizontal mesh size of $2.2\,\mathrm{km}$ (Reinert et al., 2025). The 65 height levels are terrain following near the surface and flat near the tropopause (Leuenberger et al., 2010). At this resolution, the deep convection parametrization is not active and shallow convection is parametrized using the scheme developed by Tiedtke (1989) and Bechtold et al. (2001). Turbulence is parameterized by the turbulent kinetic energy (TKE) equation of Raschendorfer (2001) and the five prognostic hydrometeor mixing ratios (cloud water, cloud ice, rain, snow and graupel) are estimated using the Lin et al. (1983) one-moment bulk microphysics scheme. Lateral boundary conditions are taken from the ICON-EU forecast ensemble that runs with parametrized convection and is updated every three hours.

2.3 The assimilation step

The assimilation step in KENDA is carried out by a Local Ensemble Transform Kalman Filter (LETKF) following Hunt et al. (2007). Its first advantage, shared with all flavors of the ensemble Kalman filter, is the flow-dependency of the background error covariance $\mathbf{P}^{\mathrm{b}} = (k-1)^{-1}\mathbf{X}^{\mathrm{b}}(\mathbf{X}^{\mathrm{b}})^{\mathrm{T}}$, where $\mathbf{X}^{\mathrm{b}(i)} = \mathbf{x}^{\mathrm{b}(i)} - \bar{\mathbf{x}}^{\mathrm{b}}$ are the background ensemble deviations, i.e. the anomalies. Its second advantage is its computational efficiency, since the analysis update is computed in the low-dimensional ensemble space

https://doi.org/10.5194/essd-2026-352
Preprint. Discussion started: 11 September 2026

Open Access Earth System Science Data Discussions

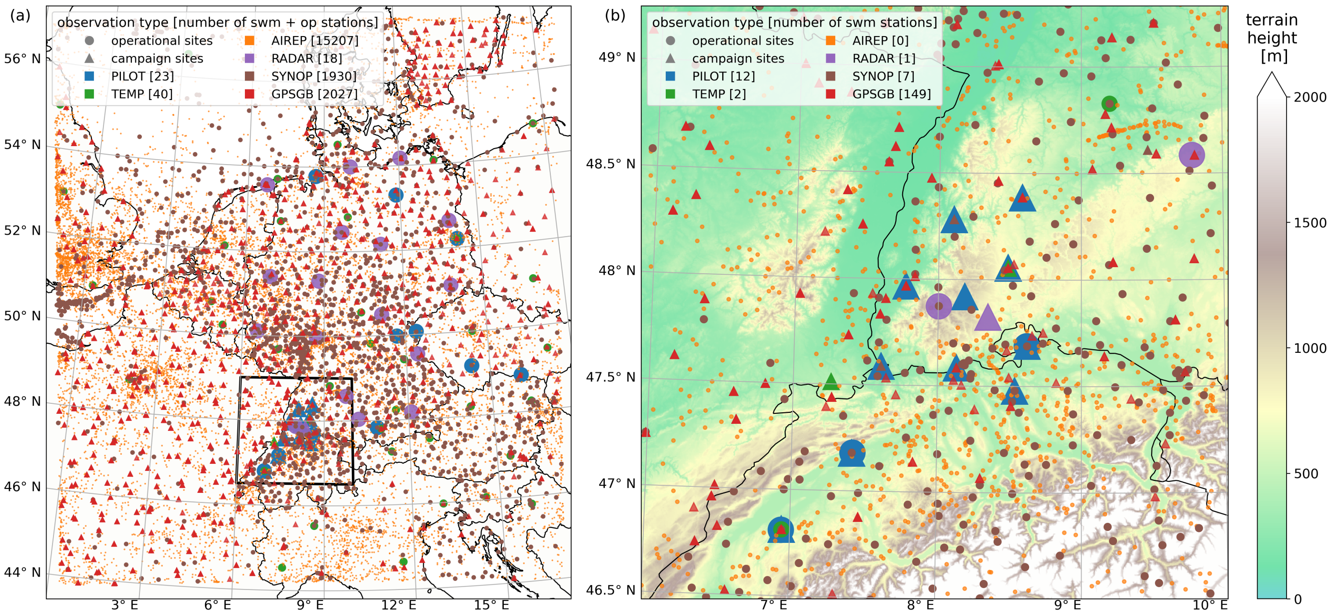

Figure 2. (a) ICON-D2 domain including sites with observations that were actively assimilated at least once during the campaign period. Operational observations (OP) are marked by circles and observations additionally used in the campaign reanalysis are marked by triangles. Shown are wind profiler (PILOT; blue), radiosounding (TEMP; green), aircraft reports (AIREP; orange), radar (RADAR; purple), surface stations (SYNOP; brown) and ground-based receivers from the Global Navigation Satellite System (GPSGB; red). The black square indicates the Black Forest (BF) domain shown in **(b)**. **(b)** Topography of the BF domain (shading; in m) centered around the campaign area, covering the Black Forest, Swabian Jura, French Vosges, and Swiss Jura mountain ranges as well as a part of the Alps. This domain was selected based on the combined observation influence of the Doppler wind lidar observations (cf. Fig. 3). Numbers in brackets in the legends denote **(a)** the total number of individual sites for each observation type and **(b)** the number of additional campaign sites in the BF domain.

of dimension $k = 40$. The analysis update is computed on a coarser rotated lat-lon grid. The LETKF minimizes a cost function depending on the weight vector $\mathbf{w}$ with dimension k. It is given by

$$J(\mathbf{w}) = (k-1)\mathbf{w}^{\mathrm{T}}\mathbf{w} + (\mathbf{y}^{\mathrm{o}} - \bar{\mathbf{y}}^{\mathrm{b}} - \mathbf{Y}^{\mathrm{b}}\mathbf{w})^{\mathrm{T}}\mathbf{R}^{-1}(\mathbf{y}^{\mathrm{o}} - \bar{\mathbf{y}}^{\mathrm{b}} - \mathbf{Y}^{\mathrm{b}}\mathbf{w}) \;, \tag{1}$$

with the diagonal observation-error variance matrix $\mathbf{R}$ and the background ensemble deviations $\mathbf{Y}^{\mathrm{b}(i)} = \mathbf{y}^{\mathrm{b}(i)} - \bar{\mathbf{y}}^{\mathrm{b}}$ in observation space. The model equivalents $\mathbf{y}^{\mathrm{b}(i)}$ are obtained by applying the non-linear forward operator $H(\mathbf{x}^{\mathrm{b}(i)})$. The cost function is minimized by the weight vector $\bar{\mathbf{w}}_0$ that can then be used to obtain the updated analysis ensemble in model space

$$\bar{\mathbf{x}}^{\mathrm{a}(i)} = \bar{\mathbf{x}}^{\mathrm{b}} + \mathbf{X}^{\mathrm{b}(i)}\bar{\mathbf{w}}_0 \;, \tag{2}$$

https://doi.org/10.5194/essd-2026-352
Preprint. Discussion started: 11 September 2026

based on the background ensemble mean $\bar{\mathbf{x}}^{\mathrm{b}}$ and the background ensemble deviations $\mathbf{X}^{\mathrm{b}(i)} = \mathbf{x}^{\mathrm{b}(i)} - \bar{\mathbf{x}}^{\mathrm{b}}$. The LETKF updates the output variables temperature T, specific humidity QV, surface pressure P, horizontal wind components U and V, cloud water QC and cloud ice QI. In addition to direct assimilation by the LETKF, during the assimilation interval, KENDA includes a latent heat nudging scheme (Stephan et al., 2008) to adjust temperature and relative humidity according to precipitation estimates from radar observations. As done operationally and described in Schraff et al. (2016), both additive (Zeng et al., 2018) and adaptive multiplicative inflation (Anderson and Anderson, 1999) as well as relaxation to prior perturbations (Zhang et al., 2004) are applied to adjust the ensemble spread.

2.4 Localization

The LETKF is 'local'in the sense that it computes the analysis ensemble at each grid point individually and includes only observations in the vicinity of each grid point, defined via horizontal and vertical localization R_{loc} and cutoff radii, and weights the observations depending on their radial distance from the grid point. The localization radius is different for each observation and is set by the adaptive localization algorithm that is part of the KENDA suite. For each grid point it only uses observations within a volume defined in the horizontal plane by a Gaspari–Cohn function $G(R_{\mathrm{loc}})$ that only depends on the localization radius $R_{\mathrm{loc}} = 2\sqrt{\frac{10}{3}}\,l_{\mathrm{loc}}$. The localization radius itself is proportional to a localization length scale l_{loc} (Gaspari and Cohn, 1999), such that the number of assimilated observations per grid point in the case of homogeneously distributed observations (such as satellite observations) with observation density ρ equals

$$N_{\mathrm{GP}} = \int_0^{r_{\mathrm{loc}}} G(r)\,\rho\,2\pi\,\mathrm{d}r \approx 2\pi\,\rho\,l_{\mathrm{loc}}^2\,. \tag{3}$$

The localization radius for conventional observations (all, except satellite, radar and GNSS) is based on an adaptive algorithm inside KENDA and can take values between $50\,\mathrm{km}$ and $100\,\mathrm{km}$ such that the number of observations influencing each grid point is roughly constant and close to 100. In the case of the Doppler wind lidar (DWL) observations assimilated in the Swabian MOSES 2023 campaign reanalysis (see Sect. 3.2), the horizontal localization radius takes the minimal value of $50\,\mathrm{km}$, due to the fact that there are many observations within a relatively small area. Figure 3 shows that the localization weights of the 12 DWLs strongly overlap and reach well beyond the Black Forest mountain range. For that reason, the BF domain is chosen such that it includes most of the influence area of the DWLs.

2.5 Observation errors

The error covariance matrix $\mathbf{R}$ is fully diagonal and includes an error estimate for each observation based on its intrinsic measurement error and the representativeness error (Janjić et al., 2018). The latter also accounts for representativity issues due to the limited resolution of the model and the instrument. The mean observation errors, evaluated over the BF domain are shown in panel (c) of Fig. 7 - 12 for the variables U, V, T, RH and $RADREFL$ (radar reflectivity). The SWM observation

https://doi.org/10.5194/essd-2026-352
Preprint. Discussion started: 11 September 2026

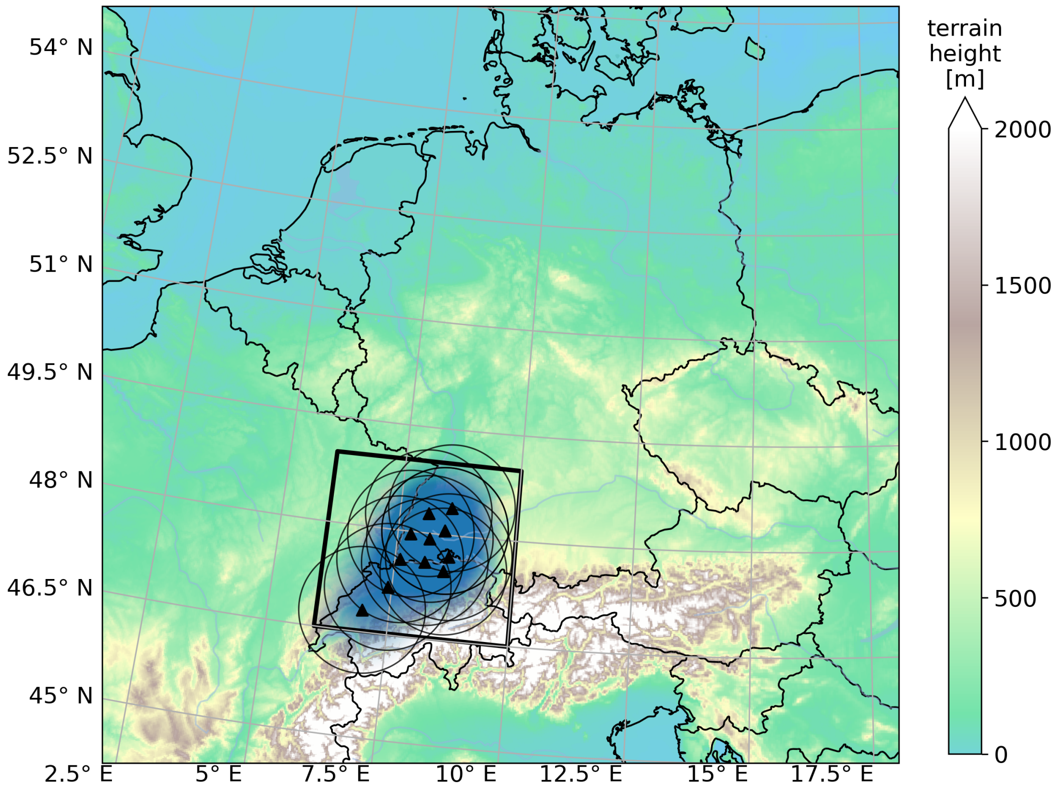

Figure 3. Locations of Doppler wind lidars (DWLs; triangles) and their localization weights (blue shading). The transparency scales with the value of the Gaspari-Cohn function with 50 km localization radius. Black circles indicate the cutoff radius. The black rectangle marks the Black Forest domain, which includes the area with significant DWL influence. The terrain shading shows the topography of the ICON-D2 domain.

errors are set identical to the OP observations of the same type and variable. This is justified (see Section 4) by comparing the a priori set observation error with the Desroziers diagnostic (Desroziers et al., 2005)

$$R_{\text{diag}} = \overline{(\mathbf{o}-\mathbf{a})\cdot(\mathbf{o}-\mathbf{b})^{\mathrm{T}}}, \tag{4}$$

calculated as the expectation value of the analysis departure $(\mathbf{o}-\mathbf{a})$ multiplied by the background departure $(\mathbf{o}-\mathbf{b})$ in observation space. The comparison is shown in panel (c) and (h) of Fig 10 - 12. Using this method, we also found the mean background and analysis error variances to be reasonable.

https://doi.org/10.5194/essd-2026-352
Preprint. Discussion started: 11 September 2026

3 Assimilated observations

The following section provides an overview of the different observations and observation types that are assimilated operationally in CTRL and added in the CMPG experiment. Table 2 summarizes the observation types and their respective variables.

Table 2. Overview of observation types and respective variables assimilated in the regional assimilation-forecasting cycle of Deutscher Wetterdienst.

observation type	**description**	**assimilated variables**
SYNOP	near-surface station	$T2M$, $RH2M$, PS
TEMP	radiosounding (ascent and descent)	T, RH, U, V, $U10M$, $V10M$, $height$
AIREP	aircraft in situ reports (AMDAR) and surveillance radar retrievals (MODE-S)	T, RH, U, V
PILOT	wind profiles (pilot balloon sounding, radar wind profiler, Doppler wind lidar)	U and V
GPSGB	ground-based GNSS receiver	ZPD
RADAR	radar volumes	$RADREFL$ and $RADWIND$
DRIBU	drifting buoys	PS, $U10M$, $V10M$
RAD	satellite radiances	$REFL$ and $RAWBT$

3.1 Operationally assimilated observations

Operationally, Deutscher Wetterdienst assimilates conventional observations as well as reflectances and brightness temperatures from the SEVIRI instrument onboard the METEOSAT second generation satellite (observation type RAD). Observations of type SYNOP (surface pressure PS, $2\,\mathrm{m}$-temperature $T2M$, $2\,\mathrm{m}$-relative humidity $RH2M$ and 10-m wind) are assimilated hourly. Operational radiosondes (observation type TEMP) are assimilated at a fixed location and typically at $0\,\mathrm{UTC}$ and $12\,\mathrm{UTC}$, and for some stations additionally at $6\,\mathrm{UTC}$ and $18\,\mathrm{UTC}$. The radiosonde profiles are assimilated at a vertical resolution of $10\,\mathrm{hPa}$ in the lower troposphere below $750\,\mathrm{hPa}$ and every $20\,\mathrm{hPa}$ above. In addition to observations during the ascent, also observations of the descent are assimilated, valid at different times and locations compared to the observations carried out during the ascent. The observation type AIREP collects airplane in situ reports (AMDAR) and airport surveillance radar retrievals (MODE-S) which both provide wind and temperature observations (Lange and Janjić, 2016). Most AMDAR and MODE-S data are available during daytime and near airports, where aircraft ascent and descent, as well as at flight level ($\sim 10\,\mathrm{km}$). Operational wind profiler data (observation type PILOT) from radar wind profilers (RWPs) are assimilated every half hour. They provide observations of the horizontal wind components with a vertical resolution of $150\,\mathrm{m}$. From the 17 operational C-band precipitation radars, radar reflectivity $RADREFL$ and radial wind $RADWIND$ are assimilated hourly when available as observation type RADAR. Near-surface observations from drifting buoys (DRIBU) are very sparse in the Germany-centered ICON-D2 domain and are therefore neglected in the subsequent analysis.

https://doi.org/10.5194/essd-2026-352
Preprint. Discussion started: 11 September 2026

3.2 Campaign observations

In CMPG, observations from the *Swabian MOSES 2023* campaign (Handwerker et al., 2025) are assimilated in addition to the operational observations. The campaign took place in JJA 2023 and targeted hydro-meteorological extremes in the southwest German Black Forest and Swabian Jura mountain ranges. The Swabian Jura presents a local maximum of hail days per year (Puskeiler et al., 2016; Fluck et al., 2021). The Black Forest, located upstream during the typical south-westerly flow conditions associated with hail days, is assumed to contribute to triggering these convective events (Kunz and Puskeiler, 2010; Handwerker et al., 2025). Similar effects have been observed over the Vosges mountains (Weckwerth et al., 2014). Although on a much larger scale, a similar hypothesized interplay between the Rocky Mountains and the high plains in the United States motivated the MPEX campaign (Weisman et al., 2015). To investigate the dynamic and thermodynamic state of the lower troposphere in the region where convection is often initiated, a dense network of instruments has been deployed in and around the southern Black Forest mountains. An extensive overview of all campaign instrumentation is presented in Handwerker et al. (2025). Here, we only describe the observations used for assimilation. The observations used for assimilation are chosen according to the capabilities of the KENDA system. Summed over three months, CMPG includes $6\,\mathrm{million}$ additional observations compared to CTRL, i.e., the number of SWM observations amount to $2.5\,\%$ of the total number of OP observations. In the BF domain, SWM observations make up $45\,\%$ of the total number of OP observations. The number of additionally assimilated observations on the BF domain per variable and altitude is shown in Fig. 4. The following sections describe the details of the assimilated Doppler wind lidar (DWL), X-Band radar, radiosounding, meteorological mast and GNSS observations.

3.2.1 Doppler wind lidar wind profiles

Ground-based DWLs provide high-resolution wind profiles of the boundary layer. In CMPG, we assimilate vertical profiles of the zonal and meridional components of the wind (U and V, respectively) retrieved from 12 DWLs. To the best of our knowledge, this DWL network presents the most comprehensive dataset used for DA experiments to date. The DWLs used here retrieve wind profiles up to approximately $3\,\mathrm{km}$ to $6\,\mathrm{km}$ above ground. The DWL range and wind profile availability depends on atmospheric conditions, i.e. aerosol availability and cloud cover (Erdmann and Gasch, 2026). Since low-level convergence is a key ingredient for the development of convection, the instruments were distributed predominantly around the Black Forest mountain range, the suspected trigger area for convective systems during the campaign. Eight DWLs from KITcube (Kalthoff et al., 2013) were located in and around the southern Black Forest (Fig. 2; blue triangles). In addition, four DWLs provided by the Swiss Meteorological Service (MeteoSwiss) were included in CMPG. The latter DWLs are operational in the MeteoSwiss forecasting system but are not yet actively assimilated at Deutscher Wetterdienst.

We assimilate DWL retrieved vertical profiles of U and V with $10\,\mathrm{min}$ temporal and $100\,\mathrm{m}$ vertical resolution at each full hour. Due to the capabilities of KENDA at the time, no vertical thinning is applied. The largest number of observations is available between $900\,\mathrm{hPa}$ and $700\,\mathrm{hPa}$ (Fig. 4b). Above $650\,\mathrm{hPa}$ (i.e. $\approx 3.5\,\mathrm{km}$), the number of DWL observations decreases rapidly. The retrieved wind profiles are assimilated as observation type PILOT (Table 2) together with wind profiles obtained

https://doi.org/10.5194/essd-2026-352
Preprint. Discussion started: 11 September 2026

Open Access Earth System Science Data Discussions

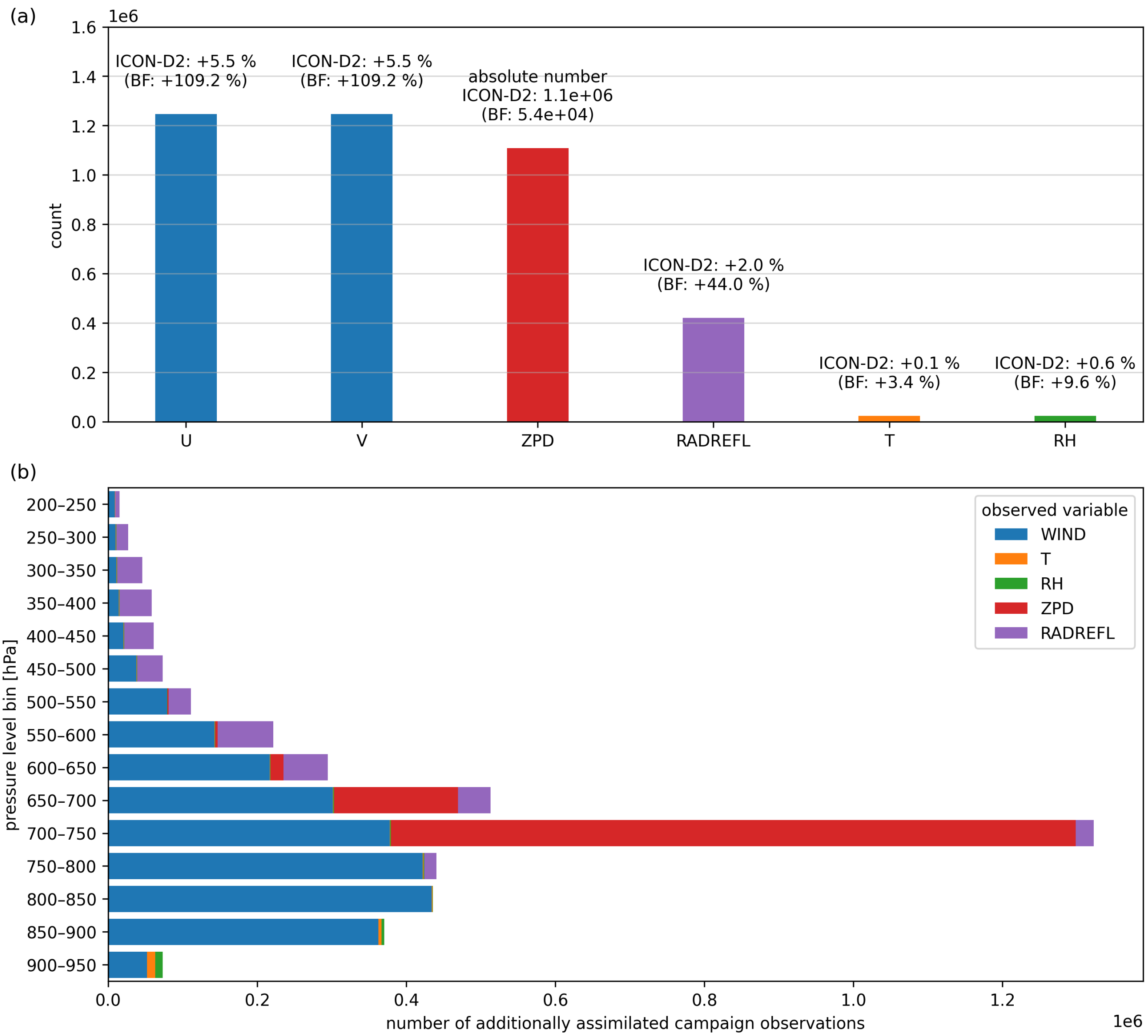

Figure 4. (a) Number of assimilated campaign observations per observed variable. Shown are observations of zonal U and meridional V wind, zenith path delay ZPD, radar reflectivity $RADREFL$, temperature T and relative humidity RH. The numbers indicate the relative increase in observation number compared to operational observations for the whole ICON-D2 domain and the smaller Black Forest domain (BF domain). For ZPD, the absolute numbers are shown. **(b)** Vertical profile of the number of assimilated campaign observations shown above. Wind includes all U and V observations.

https://doi.org/10.5194/essd-2026-352
Preprint. Discussion started: 11 September 2026

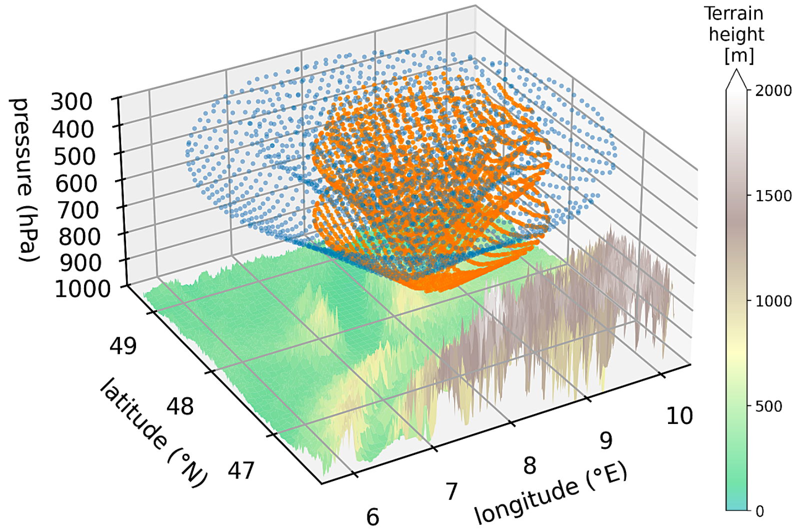

Figure 5. Assimilated radar reflectivity points in observation space for the SWM X-band (orange) and operational C-band (blue) radars located in the Black Forest. The shading shows the underlying topography ranging up to $1050\,\mathrm{m}$ a.s.l. The localization radius is $16\,\mathrm{km}$ around each of the scatter points.

from operational RWPs, which are mostly distributed in the northwestern region of the ICON-D2 domain and at three locations in Switzerland (Fig. 2; blue circles).

3.2.2 X-Band radar volumes

KITcube's mobile scanning X-band precipitation radar (Kalthoff et al., 2013) was installed in the southern Black Forest nearly in the center of the campaign domain (Fig. 2; purple triangle and Fig. 5; orange dots) and covered the whole campaign area at low elevation angles. Due to an initial malfunction, it only acquired data from 11 July 2023 onward. From the intensity and the Doppler shift of the $\sim 3\,\mathrm{cm}$ wavelength signal, radar reflectivity ($RADREFL$) and Doppler velocity ($RADWIND$) can be derived. Since the test-wise assimilation of $RADWIND$ showed a height-dependent bias, likely related to insufficient data postprocessing of folded radial velocities, $RADWIND$ was excluded. $RADREFL$ has been actively assimilated from 12 July 2023 until the end of August 2023, and provides the largest number of assimilated campaign observations during rainy days (not shown). Following the operational setup, all radar observations are spatially superobbed to a horizontal resolution of $5\,\mathrm{km}$ and temporally thinned to only assimilate data from the latest $5\,\mathrm{min}$ before the analysis time. Reflectivity observations with values below $0\,\mathrm{dBz}$ are not assimilated. Since the volumes of the campaign X-band radar and the operational C-band radar largely overlap (Fig. 5), their influence on the analysis can be easily compared (see Sect. 4).

https://doi.org/10.5194/essd-2026-352
Preprint. Discussion started: 11 September 2026

3.2.3 Radiosoundings

During intensive observation periods (IOPs) additional radiosondes were launched at two sites: At a site upstream of the Black Forest in Kœstlach (KOE), France, and at the main site in Villingen-Schwenningen (VS), Germany (Fig. 2; green triangles). During each IOP, radiosondes have been released every six hours in KOE and every three hours in VS. Eight such IOPs were carried out during June and July 2023 and nearly 200 radiosondes were launched in total (Handwerker et al., 2025). Although this amount of soundings increases the number of sounding observations in the BF domain by two-thirds (around $9 \cdot 10^3$ SWM observations and around $14 \cdot 10^3$ OP observations per variable) during the campaign period, for wind profiles this number is still very low compared to the number of U and V observations obtained from the DWLs (around $1.2 \cdot 10^6$ each, Fig. 4a). Radiosonde observations are vertically thinned according to Deutscher Wetterdienst's operational procedure described in Section 3.1. Operational radiosoundings are included in CTRL and CMPG, while radiosoundings from KOE and VS are included in CMPG only.

3.2.4 Meteorological mast observations

Six meteorological masts were deployed during the campaign (Fig. 2; brown triangles), from which $2\,\mathrm{m}$-temperature ($T2M$) and $2\,\mathrm{m}$-relative humidity ($RH2M$) are assimilated. Surface pressure observations are excluded due to observational biases resulting from uncalibrated instruments. In addition, $T2M$ observations at the site in Titisee are excluded due to a strong nighttime model warm bias (not shown), which is most likely caused by insufficiently resolved topography. Similar effects were also observed in assimilation and model verification studies in the Alps where topographic cold pools are systematically underrepresented (e.g., Bugnard et al., 2025).

3.2.5 GNSS zenith path delays

Ground-based Global Navigation Satellite System (GNSS) receivers measure the delay of GPS signals. The total path delay depends on pressure, temperature and humidity (Bevis et al., 1992; Thundathil et al., 2024). GNSS observations are not yet assimilated operationally in Deutscher Wetterdienst's regional NWP system. For this reason, the SWM observation set includes GNSS zenith path delay (ZPD; equivalent to zenith total delay ZTD) observations on the full domain, in addition to the sites installed specifically for the campaign (Fig. 2; red triangles). Since the LETKF requires every single observation to be assigned to a location, each ZPD observation is attributed to a single level at $2000\,\mathrm{m}$ above the receiver station. This height is chosen such that the observations have a positive impact. For the GNSS assimilation, an online bias correction is applied, as ZPD observations from different countries and different stations have different biases. The bias stabilizes after approximately two weeks. Therefore, the full number of observations is only used from 14 June 2023 onward. Overall, CMPG assimilates roughly 600 ZPD observations per hour in the ICON-D2 domain.

https://doi.org/10.5194/essd-2026-352
Preprint. Discussion started: 11 September 2026

4 Observation space evaluation

Evaluation formulation

In this section, we characterize the mean and standard deviation of the difference between assimilated observations and the model before and after assimilation. This is performed in so-called observation space, where the model can be compared to the observations at the time step and location at which they were taken. We evaluate each variable of which there are additional observations assimilated in CMPG (Section 3.2). Every such model equivalent is computed using a forward operator. If the observed variable itself is also a model field, the forward operator is an interpolation to the time and location when and where the observation was taken. On top of the spatiotemporal interpolation, the model equivalents for ZPD und $RADREFL$ are obtained by also applying a specific nonlinear forward operator, e.g., EMVORADO (Zeng et al., 2016) for $RADREFL$. We shall refer to the difference between a single observation, o, and the model equivalent of the background in observation space, b, as the **background departure**, $o-b$. The difference between observation o and the model equivalent of the analysis a in observation space is called **analysis departure**, $o-a$. In the computation of the departures, we only use the deterministic model output and not the ensemble members. The departures are evaluated statistically using the mean of the background and analysis departures, $\overline{(\mathbf{o}-\mathbf{b})}$ and $\overline{(\mathbf{o}-\mathbf{a})}$, and the standard deviations, $\mathrm{std}(\mathbf{o}-\mathbf{b})$ and $\mathrm{std}(\mathbf{o}-\mathbf{a})$. In the following, these statistics are computed separately for each of the variables U, V, T, RH, and $RADREFL$, and separately for SWM and OP observations. All observation space statistics are based on the CMPG reanalysis that includes SWM and OP observations. Ideally, data assimilation should reduce the mean absolute difference between observations and their model equivalents. Given that model biases are typically much smaller than the root mean square error, data assimilation should also reduce the standard deviation of the departures

$$\mathrm{std}(\mathbf{o}-\mathbf{a}) < \mathrm{std}(\mathbf{o}-\mathbf{b})\ . \tag{5}$$

In the following, we will also evaluate whether data assimilation reduces the mean difference between observations and their model equivalents, i.e., if

$$\overline{(\mathbf{o}-\mathbf{a})} < \overline{(\mathbf{o}-\mathbf{b})}\ . \tag{6}$$

Furthermore, the observation error, ϵ_o, set a priori in KENDA for each observed variable and each height level (Section 2) is compared with the error estimate $R_\mathrm{diag} = \overline{(\mathbf{o}-\mathbf{a})(\mathbf{o}-\mathbf{b})^\mathrm{T}}$ based on Desroziers et al. (2005). If the background error covariance matrix B is correctly specified, ϵ_o should match R_diag. However, this is not the case in reality, and, thus, R_diag is only a rough estimate, but can still be used after some iterations. Using this error diagnostic, one can empirically identify the optimal ϵ_o profile for each observed variable and each observation type. Since changing ϵ_o has a large influence on the weights in the Kalman filter equation (Eq. 1), it is not always tuned to perfectly match R_diag. Therefore, in the following evaluation, we consider it a good result if R_diag for SWM and OP (i.e., campaign and operational observations) is fairly similar and of the same order of magnitude as ϵ_o.

https://doi.org/10.5194/essd-2026-352
Preprint. Discussion started: 11 September 2026

Open Access Earth System Science Data Discussions

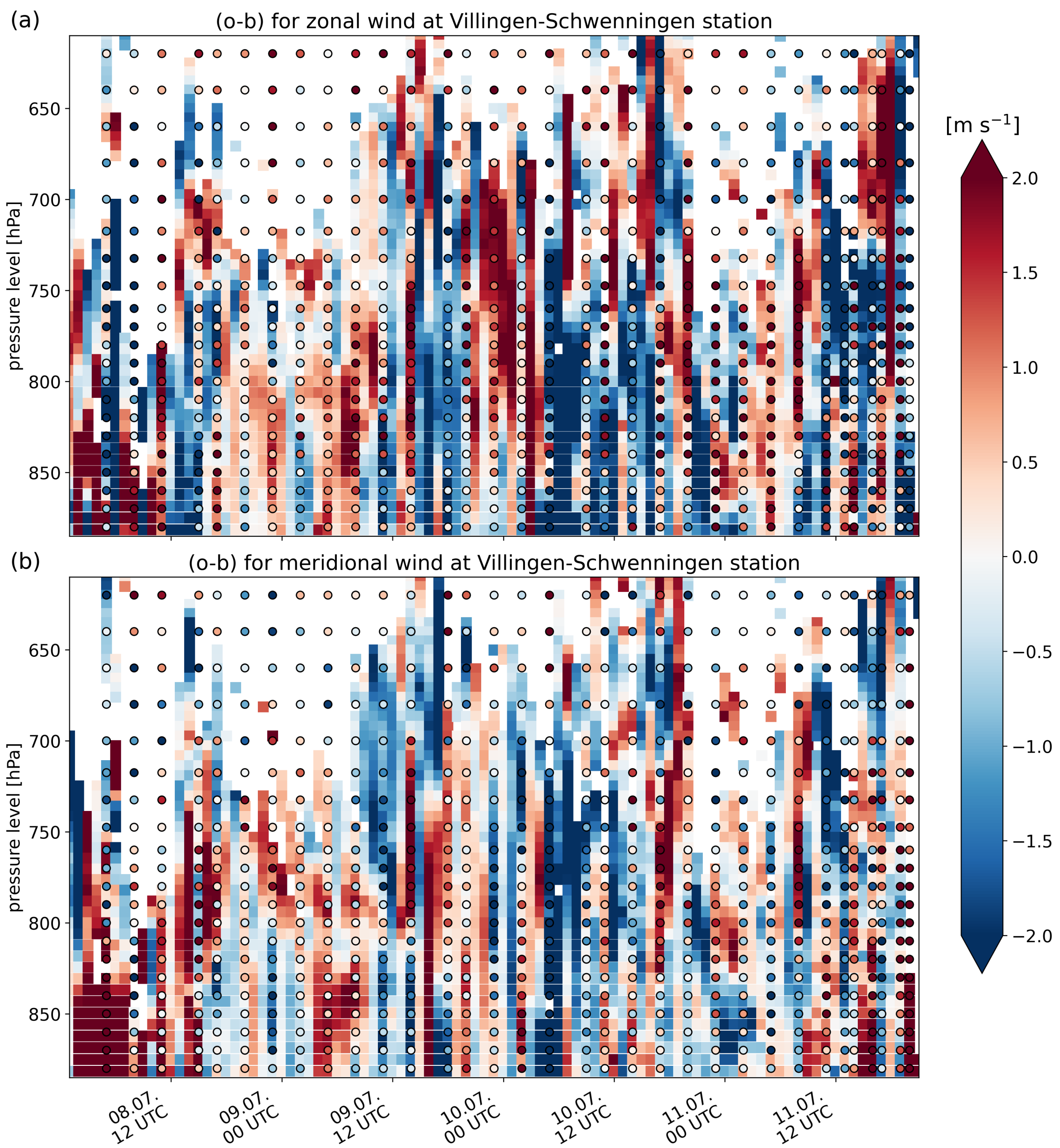

Figure 6. (a) Background departure $(o-b)$ of zonal wind during four exemplary days of the campaign. Each symbol represents one individual assimilated observation, either from radiosonde (circles) launched at Villingen-Schwenningen (VS) or from the Doppler wind lidar located at VS (squares in the background). **(b)** same as **(a)** but for meridional wind.

4.1 Horizontal wind

4.1.1 Exemplary background departure timeseries in observation space

Figure 6 shows an exemplary timeseries of $(o-b)$ during four IOP days. It mainly shows that the high temporal variability of $(o-b)$ calls for a statistical analysis of the departures that accounts for the entirety of observations. In Fig. 6, each scatter point corresponds to a single assimilated observation. Squares show the $(o-b)$ values of the DWL placed at VS and circles show the $(o-b)$ values of the radiosondes launched in VS. While the radiosonde typically ascends to the top of the troposphere, DWL wind retrievals are only available if sufficient aerosol is available and the signal is not extinguished by clouds or precipitation. Furthermore, strong precipitation also limits the data availability. Figure 6 only shows the $(o-b)$ values below $650\,\mathrm{hPa}$ pressure level, since above this level the number of DWL observations decreases rapidly. The background departures for radiosonde and DWL retrieved wind profiles are expected to match in the lowest part of the troposphere and differ higher up, where the radiosonde has drifted away substantially from its launching location and the observation time difference between radiosonde and DWL retrieval increases. This expectation is met at some time steps (e.g. zonal and meridional wind on 9 July 2023), but there are instances at which the sign of $(o-b)$ is opposite for DWL and radiosonde observations (e.g. zonal wind on 10 July 2023, 21 UTC and meridional wind on 8 July 2023, 15 UTC; red circles on blue squares). While radiosonde observations are in situ measurements, sampling one instance in space and time, the DWL retrievals are $10\,\mathrm{min}$ averages retrieved from a volume explored by the scan pattern. It is expected that the DWL retrievals cannot resolve the short-term variability of the flow in convective situations with strong wind gusts. Additionally, the DWL wind profile retrieval error may be increased during strongly turbulent conditions. A validation by Erdmann and Gasch (2026) supports this argument. They find an up to $-0.4\,\mathrm{m\,s^{-1}}$ slow bias in the wind speed of the DWL at VS, i.e. faster zonal winds measured by the radiosonde. They argue that this bias may be due to gusts, which are not fully resolved in the DWL measurements, and show that reducing the averaging time (from $10\,\mathrm{min}$ to $5\,\mathrm{min}$) slightly reduces the bias.

4.1.2 Zonal wind

As shown in Fig 4a, most of the additionally assimilated observations in CMPG are zonal and meridional wind components, U and V. These are assimilated from observation types AIREP, TEMP and PILOT (see Section 3.2 for details). The largest number of wind observations in the BF domain are DWL measurements from the Swabian MOSES 2023 campaign, assimilated as observation type PILOT mostly below $700\,\mathrm{hPa}$ (Fig. 7a and Fig. 8a; blue line). The number of U and V observations is identical (Fig. 7a and Fig. 8a). Due to the different vertical distribution of the number of observations, the mean ϵ_o (Fig. 7h and Fig. 8h) varies slightly between different observation types, although the vertical ϵ_o profiles (Fig. 7c and Fig. 8c) are identical.

The mean observed vertical profiles of zonal wind (Fig. 7b) all show an increase of U with height. Overall, TEMP U values are larger than those of PILOT and AIREP, due to sampling effects discussed in Sect. 4.1.4. The meridional wind component V increases up to approximately $750\,\mathrm{hPa}$, depending on the observation type, and varies slightly more among observation types than the zonal wind (Fig. 8b). The dominant flow direction during JJA 2023 was westerly to southwesterly flow. For both U and V the Desroziers estimate R_diag fits ϵ_o very well and is similar to OP (Fig. 7c,h and Fig. 8c,h; blue and black lines). Although

https://doi.org/10.5194/essd-2026-352
Preprint. Discussion started: 11 September 2026

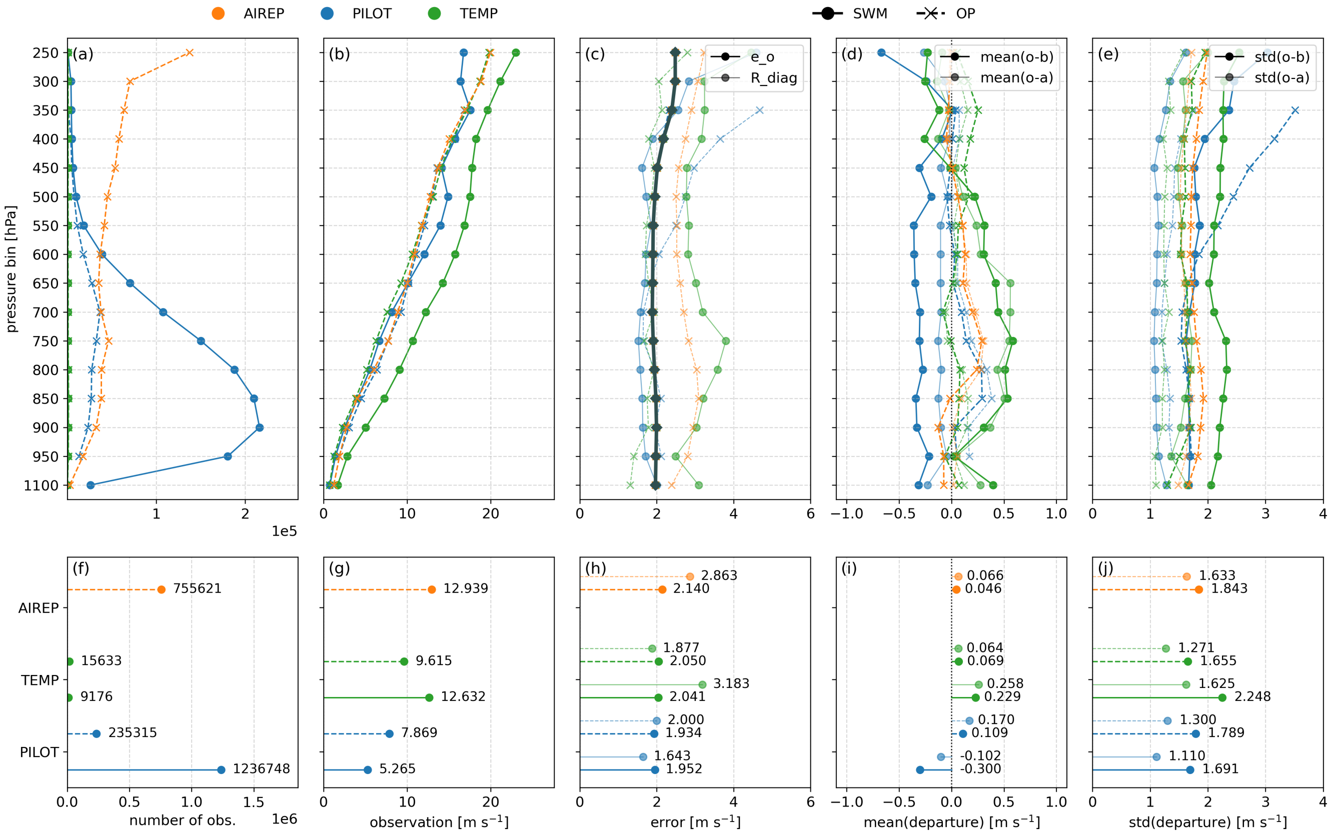

Figure 7. Observation space statistics for zonal wind (U), evaluated on the BF domain (see Fig. 2) for the three months of the campaign. **(a-e)**: Vertical profiles of observation space statistics in $50\,\mathrm{hPa}$ intervals. **(f-j)**: Vertically integrated observation space statistics for SWM (solid lines) and OP observations (dashed lines) for the various observation types (AIREP: orange; PILOT: blue; TEMP: green). **(a,f)**: Number of observations. **(b,g)**: Mean observed value. **(c,h)**: Mean value of the prescribed observation error ϵ_o in KENDA (thick and dark shaded lines) and corresponding error estimate (thin and light shaded lines), the element of R_{diag}, based on Desroziers statistics (see Sect. 2.5 for details). Note that ϵ_o has the identical vertical profile for all three observation types (thick black line). **(d,i)**: Mean background departure $\overline{(\mathbf{o}-\mathbf{b})}$ (thick and dark shaded lines) and mean analysis departure $\overline{(\mathbf{o}-\mathbf{a})}$ (thin and light shaded lines). **(e,j)**: As panels **(d,i)**, but for the standard deviation of the departures $\mathrm{std}(\mathbf{o}-\mathbf{b})$ and $\mathrm{std}(\mathbf{o}-\mathbf{a})$.

https://doi.org/10.5194/essd-2026-352
Preprint. Discussion started: 11 September 2026

the standard deviation of the departures are similar for all observation types and both U and V (Fig. 7j and Fig. 8j), there is a model bias with opposite directions for U and V as well as between PILOT and TEMP observations (Fig. 7i and Fig. 8i; blue versus green lines). Operational PILOT and TEMP observations (Fig. 7d, dashed lines) show on average a slow wind bias, i.e. the modeled U is slower than the observed U, in contrast to DWL campaign observations (Fig. 7d; blue solid lines), which reveal a positive zonal wind bias. This is not only the case for the vertically averaged mean, but also for most height bins individually, and most pronounced for SWM observations (Fig. 7d; solid blue and green lines). However, the opposite biases are within the measurement error of the wind profilers and can be due to many reasons: DWLs and RWPs retrieve the wind components from radial wind speed measurements at different azimuths and elevation angles, assuming stationarity during one scan. Due to the probed volume, they are less sensitive to gusts than the radiosondes. Moreover, since RWP scans are averaged over about $30\,\mathrm{min}$ and DWL scans are averaged over $10\,\mathrm{min}$, they do not only sample different volumes of air but also different time periods. In addition, RWPs are sensitive to precipitation and bird migration, possibly yielding disturbed wind profiles, while the DWL wind profile retrieval quality depends mainly on flow homogeneity within the retrieval volume and scan geometry (Gasch et al., 2020; Rahlves et al., 2022; Robey and Lundquist, 2022). The large number of DWL observations gives them much weight, such that $\overline{(\mathbf{o}-\mathbf{a})}$ is less negative than $\overline{(\mathbf{o}-\mathbf{b})}$ for SWM PILOT observations, but in all other cases $\overline{(\mathbf{o}-\mathbf{a})}$ is larger than $\overline{(\mathbf{o}-\mathbf{b})}$. That means, data assimilation reduces the model bias when compared to the DWL observations, thereby increasing the model bias with respect to the RWP observations inside the BF domain. Overall, the standard deviation of the departures for U and V is reduced by data assimilation for all observation types and both observation sources (SWM and OP), with an almost $35\,\%$ reduction from std$(\mathbf{o}-\mathbf{b}) = 1.691\,\mathrm{m\,s^{-1}}$ to std$(\mathbf{o}-\mathbf{a}) = 1.10\,\mathrm{m\,s^{-1}}$ for SWM PILOT (Fig. 7j; solid blue bars). This means, assimilating additional observations reduces the difference between observations and model equivalents and thus reduces the model error, given that the disagreement between PILOT and TEMP observations is smaller than the model deviations, i.e. the observations are trustworthy. This has been validated for two DWL stations in Erdmann and Gasch (2026). Section 5 shows how this local influence of the additional campaign observations spreads out in model space.

4.1.3 Meridional wind

Meridional wind shows very small background and analysis departures up to the $800\,\mathrm{hPa}$ pressure level, indicative for little systematic error for V (Fig. 8d). However, above $800\,\mathrm{hPa}$, the DWL observations reveal a model slow bias that is increasing with height. For observation type PILOT, the mean departures have the same sign for both OP and SWM observations, but SWM TEMP has a negative $\overline{(\mathbf{o}-\mathbf{b})}$ between $800\,\mathrm{hPa}$ and $400\,\mathrm{hPa}$ (Fig. 8d,i). However, on the height intervals with most V observations, the model bias is less than $0.5\,\mathrm{m\,s^{-1}}$ and therefore of comparable size as the bias in U. The values for std$(\mathbf{o}-\mathbf{b})$ and std$(\mathbf{o}-\mathbf{a})$ are also of similar size for U and V observations (Fig. 8e,j), showing that overall assimilation reduces the model wind error with respect to all observation types.

https://doi.org/10.5194/essd-2026-352
Preprint. Discussion started: 11 September 2026

Open Access Earth System Science Data Discussions

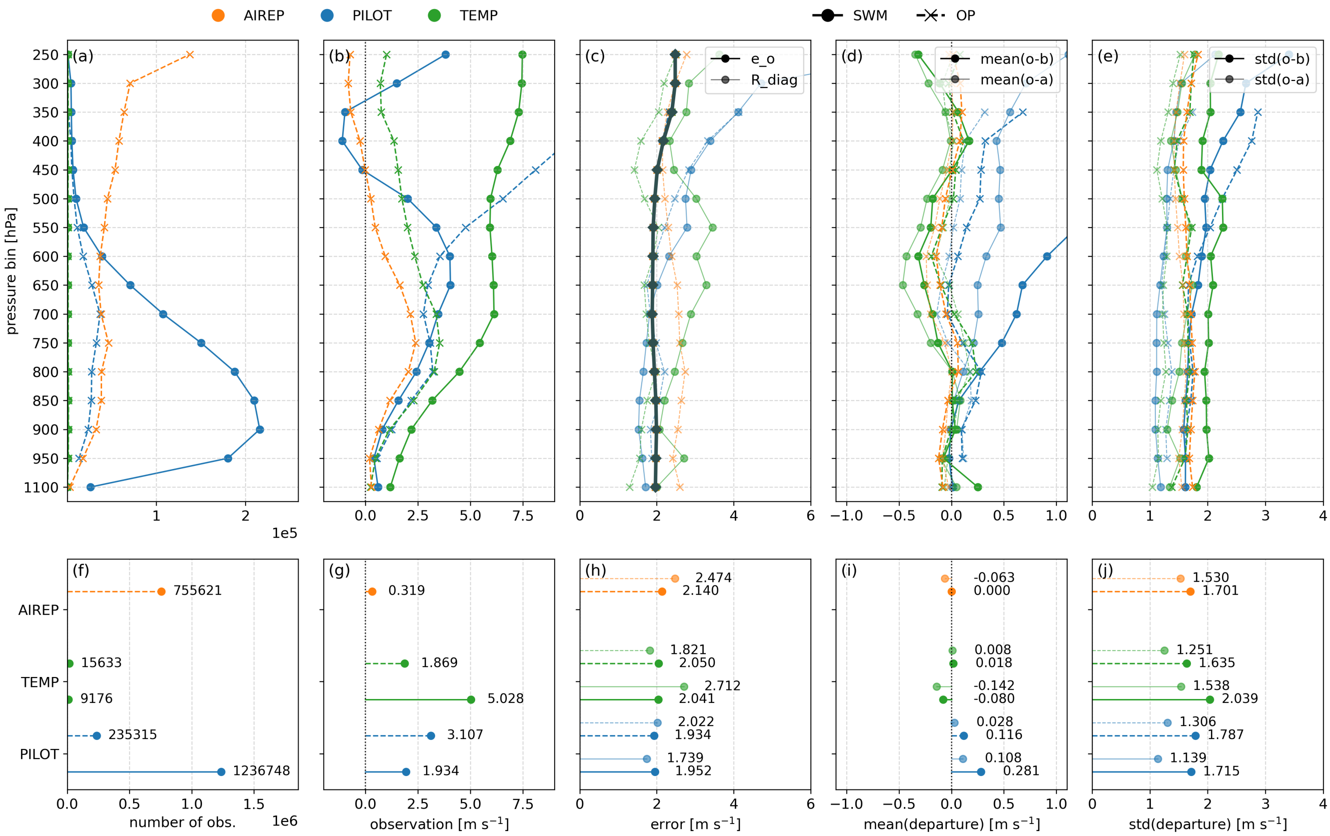

Figure 8. As Fig. 7 but for meridional wind (V).

4.1.4 Tracing differences between TEMP and PILOT during IOPs

The difference in the $\overline{(\mathbf{o}-\mathbf{b})}$ signals of U and V between SWM TEMP and SWM PILOT observations is due to the fact that they sample different synoptic situations and that each mean profile is an average over different sites. As described in Section 3.2, SWM radiosondes were only launched during intensive observation periods, targeted to sample convective situations. There are only around 100 time steps when SWM radiosondes from Villingen-Schwenningen (VS) were assimilated, whereas DWL observations are available at almost every hourly time step during JJA 2023, i.e. at more than 2000 time steps. To make the two samples comparable, we evaluate observation space statistics for each DWL (Fig. 9; red and blue lines) and the VS radiosounding station (Fig. 9; green line) individually and for only those times when radiosounding observations from VS are available. Since the vertical resolution of most DWL sites (except the one at VS because it is of a different instrument type) is higher than the vertical resolution of the radiosonde profiles after thinning, the number of U and V observations from DWLs is larger than the number from the VS radiosounding station, even if we sample exactly the same assimilation time steps (Fig. 9a,f). The IOP time steps are mostly characterized by convective conditions and southwesterly flow (Fig. 9g), leading to

https://doi.org/10.5194/essd-2026-352
Preprint. Discussion started: 11 September 2026

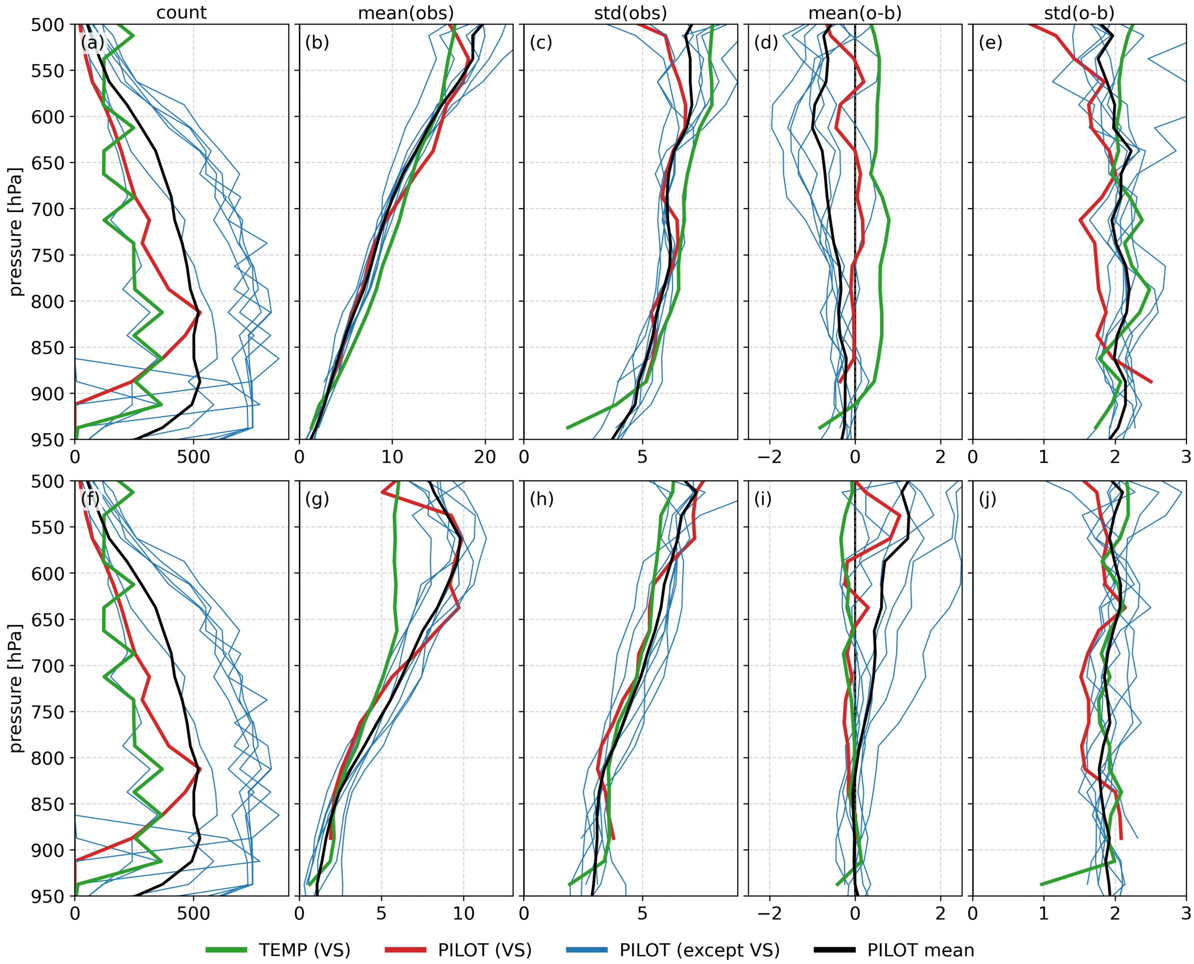

Figure 9. Observation space statistics for zonal wind (**a-e**; U) and meridional wind (**f-j**; V), evaluated on the BF domain (see Fig. 2) for the subset of time steps when observations from the Villingen-Schwenningen (VS) radiosonde are assimilated. Since U and V are retrieved together, the number statistics in **(a)** and **(f)** are identical. The red line shows the profile of the Doppler wind lidar (DWL) in VS, and the blue lines show the profiles of the remaining DWL instruments. The black line shows the mean profile of all DWL stations. **(b,g)** mean observed profile. **(c,h)** observation standard deviation. **(d,i)** mean background departure. **(e,j)** standard deviation of background departure. x-axis values for mean and std are given in $m\,s^{-1}$.

https://doi.org/10.5194/essd-2026-352
Preprint. Discussion started: 11 September 2026

a considerable drift of the sounding balloon at some time steps. Even if comparing the TEMP with PILOT observations at the same site (VS), a representativity issue is evident.

The vertical profile of the standard deviation of observation (Fig. 9c,h) and background departure (Fig. 9e,j) are similar for all stations and both observation types, but have overall larger values than in Fig. 7e,j and Fig. 8e,j. This might be due to the sampling of convective conditions during IOPs and highlights the importance of data assimilation in these conditions. The mean background departure (Fig. 9d,i) shows a clear difference between the VS station (green and red lines) and the remaining stations (blue lines). Above $700\,\mathrm{hPa}$, the spread of the $\overline{(\mathbf{o}-\mathbf{b})}$ profile for PILOT increases drastically and while the PILOT mean $\overline{(\mathbf{o}-\mathbf{b})}$ reaches values of about $-1\,\mathrm{m\,s^{-1}}$ for U and about $1\,\mathrm{m\,s^{-1}}$ for V, the $\overline{(\mathbf{o}-\mathbf{b})}$ for the VS PILOT station is close to $0\,\mathrm{m\,s^{-1}}$ at every height level for U as well as for V. This detailed evaluation shows that although $\overline{(\mathbf{o}-\mathbf{b})}$ has different signs for SWM TEMP and SWM PILOT observations, the DWL profile at VS is closest to the VS radiosonde profile. The remaining discrepancy, i.e. $\overline{(\mathbf{o}-\mathbf{b})} \approx 0\,\mathrm{m\,s^{-1}}$ for U in the case of the VS DWL and $\overline{(\mathbf{o}-\mathbf{b})} \approx 1\,\mathrm{m\,s^{-1}}$ in the case of the VS radiosonde (Fig. 9d) supports the results of Erdmann and Gasch (2026): The DWL retrieval smooths out individual gusts in convective conditions and therefore the radiosonde typically measures higher U values. This leads – in convective situations – to an underestimation of modeled U when compared to TEMP (radiosoundings) but an overestimation when compared to PILOT (DWL).

4.2 Temperature

The largest number of T observations is available from MODE-S measurements in the upper troposphere and lower stratosphere (Fig. 10a,f; orange). Campaign observations from radiosoundings (Fig. 10a,f; green) are roughly $40\,\%$ of the total number of TEMP observations in the BF domain. The number of observations of the five campaign surface sites (Fig. 10a,f; brown solid) is approximately one order of magnitude lower than the number of operational SYNOP stations (Fig. 10a,f; brown dashed). The vertical temperature profiles (Fig. 10b) as well as the overall mean observed temperatures (Fig. 10g) agree well within the three observation types. The Desroziers estimate R_{diag} is similar to ϵ_{o} for the observation types AIREP and SYNOP (Fig. 10c,h), but is less than half of ϵ_{o} for observation type TEMP for both OP and SWM observations. However, while the vertical profiles of R_{diag} and ϵ_{o} have similar shapes as for TEMP and SYNOP observations, the AIREP R_{diag} matches ϵ_{o} only when averaged vertically. Specifically, differences between ϵ_{o} and R_{diag} exist below $500\,\mathrm{hPa}$. Most importantly, R_{diag} of SWM does not differ substantially from R_{diag} of OP. This justifies the use of the quasi-operational ϵ_{o} for the SWM observations.

The mean departures (Fig. 10d,i) all show a lower tropospheric model cold bias with $\overline{(\mathbf{o}-\mathbf{b})} \approx 0.25\,\mathrm{K}$. That means, the model background is too cold compared to the observations and thus the temperature is increased through the assimilation, resulting in lower analysis departures. If averaged vertically, the largest background departures are from OP TEMP observations (Fig. 10i, green dashed). The vertically averaged SWM TEMP background departures have a rather small bias (Fig. 10i, green solid), but the vertical profile (Fig. 10d, green) shows that they are characterized by a model warm bias with $\overline{(\mathbf{o}-\mathbf{b})} \approx -0.25\,\mathrm{K}$ in the middle troposphere, which is not present in the OP TEMP observations. Differences between OP and SWM observations can result from the different locations and most probably from a sampling bias, as SWM TEMPs are only available during IOPs, targeting mostly convective conditions. For SYNOP, the model surface cold bias is more pronounced in the SWM

https://doi.org/10.5194/essd-2026-352
Preprint. Discussion started: 11 September 2026

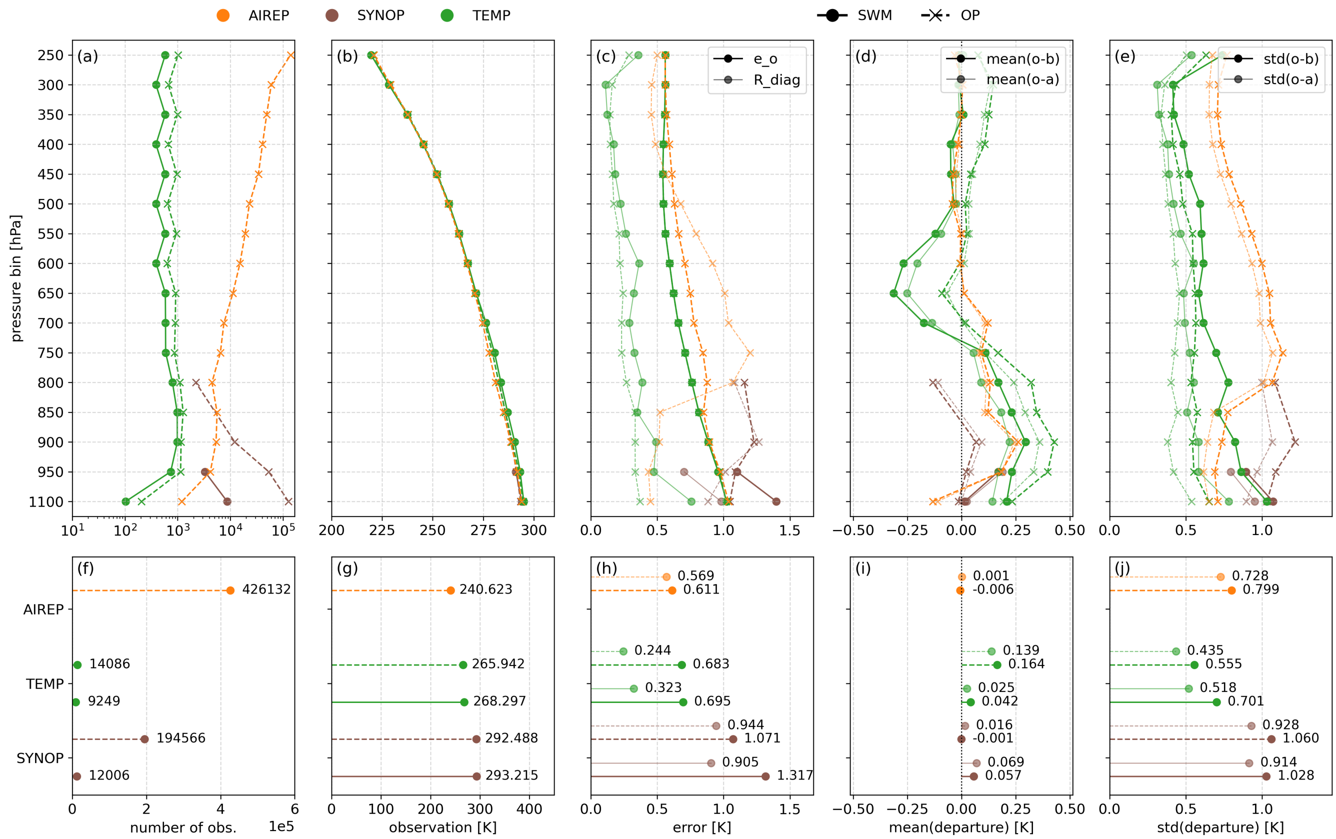

Figure 10. As Fig. 7 but for temperature (T). Notice the logarithmic x-axis in **(a)**.

observations than in the OP observations (Fig. 10d, brown). This can be due to the fact, that the campaign sites are mostly located in complex terrain, which is poorly resolved by the ICON-D2 grid and therefore cannot sufficiently represent small scale temperature variations such as nighttime cold pools. For both SWM and OP SYNOP observations, the model is warmed after assimilation (Fig. 10d,i; light brown values are larger than dark brown values). The AIREP observations show a less pronounced model cold bias in the lower troposphere (Fig. 10d; orange). This cold bias decreases with height, as the number of assimilated AIREP observations increases and yields an overall very small bias of $\overline{(\mathbf{o}-\mathbf{b})} \approx -0.006\,\mathrm{K}$ (Fig. 10i; orange). The standard deviation of the departures (Fig. 10e,j) is between $0.4\,\mathrm{K}$ and $1.1\,\mathrm{K}$ for SWM and OP observations. For all three observation types, the departures are improved after assimilation, i.e. $\mathrm{std}(\mathbf{o}-\mathbf{a}) < \mathrm{std}(\mathbf{o}-\mathbf{b})$. In particular, the improvement in the standard deviation of the temperature departures from SWM radiosoundings is $26\,\%$. This holds also for each vertical bin individually and shows that assimilating SWM temperature observations has a positive influence on the analysis.

https://doi.org/10.5194/essd-2026-352
Preprint. Discussion started: 11 September 2026

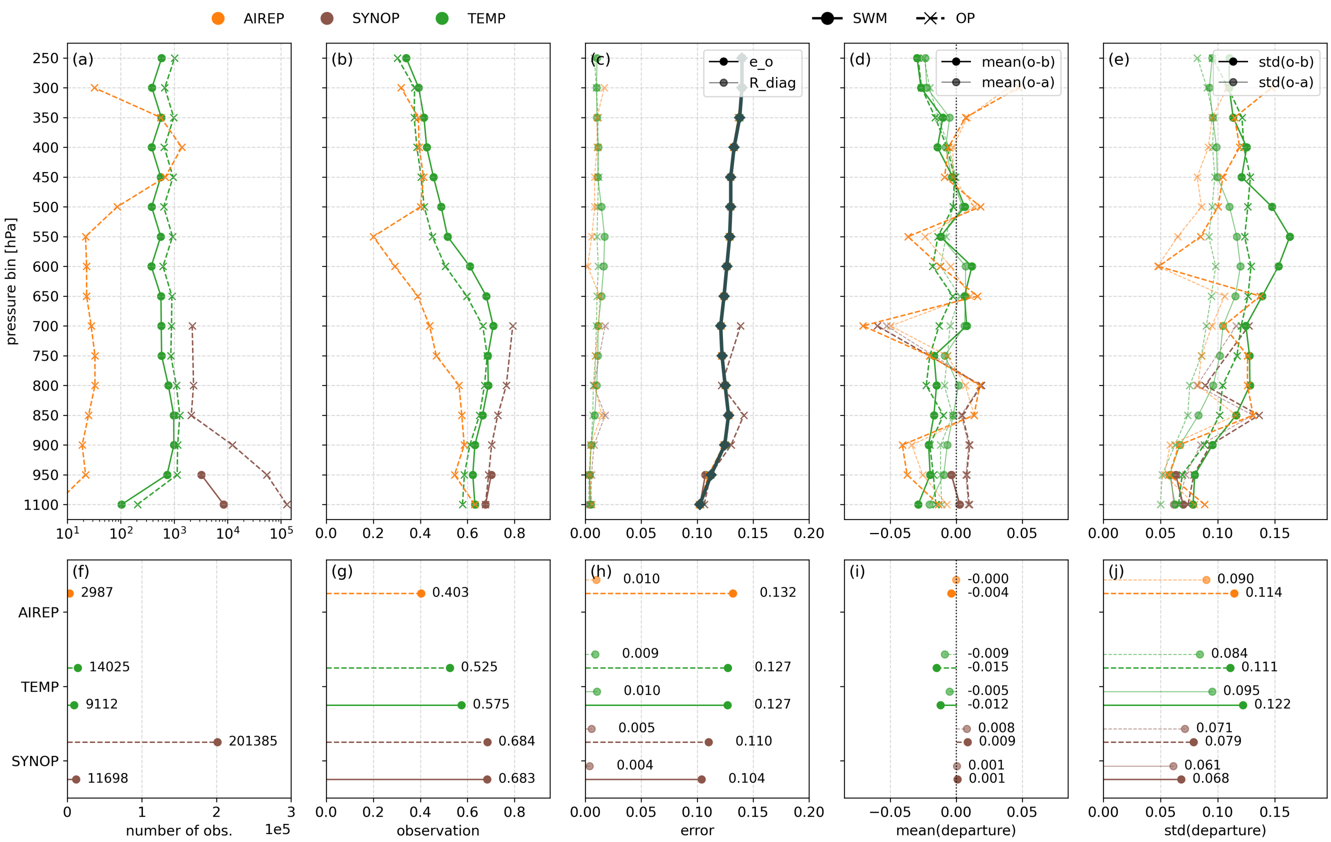

Figure 11. As Fig. 7 but for relative humidity (RH). Notice the logarithmic x-axis in **(a)**.

4.3 Relative humidity

The number of RH observations by radiosondes in the BF domain is, as expected, identical to the number of T observations (Fig. 11a; green). Similarly, the number of RH SYNOP observations is similar to the number of T SYNOP observations, too (Fig. 11a; brown). However, there are much fewer RH observations by aircraft, resulting in noisier statistics (Fig. 11a; orange). The differences between ϵ_o and R_{diag} in the case of RH are surprisingly large (Fig. 11c). R_{diag} is less than $10\,\%$ of ϵ_o for all observation types. Yet, OP and SWM observations show very similar values of R_{diag}, again justifying the use of operationally prescribed errors ϵ_o. Background departures from both SWM and OP TEMP observations show a model moist bias below $700\,\mathrm{hPa}$ (Fig. 11d; green). This model moist bias is improved through data assimilation, resulting in analysis departures being closer to zero than the background departures (Fig. 11i; green). Assimilating TEMP observations therefore cause the model to get drier at these locations, mostly below $750\,\mathrm{hPa}$. This drying might be affected by the influence of T observations: Warming the model while keeping the moisture content fixed results in lower relative humidity values. Opposite to TEMP, the OP SYNOP observations show a slight model dry bias (positive $\overline{(\mathbf{o}-\mathbf{b})}$). As for T, std$(\mathbf{o}-\mathbf{a})$ is lower than std$(\mathbf{o}-\mathbf{b})$, showing

https://doi.org/10.5194/essd-2026-352
Preprint. Discussion started: 11 September 2026

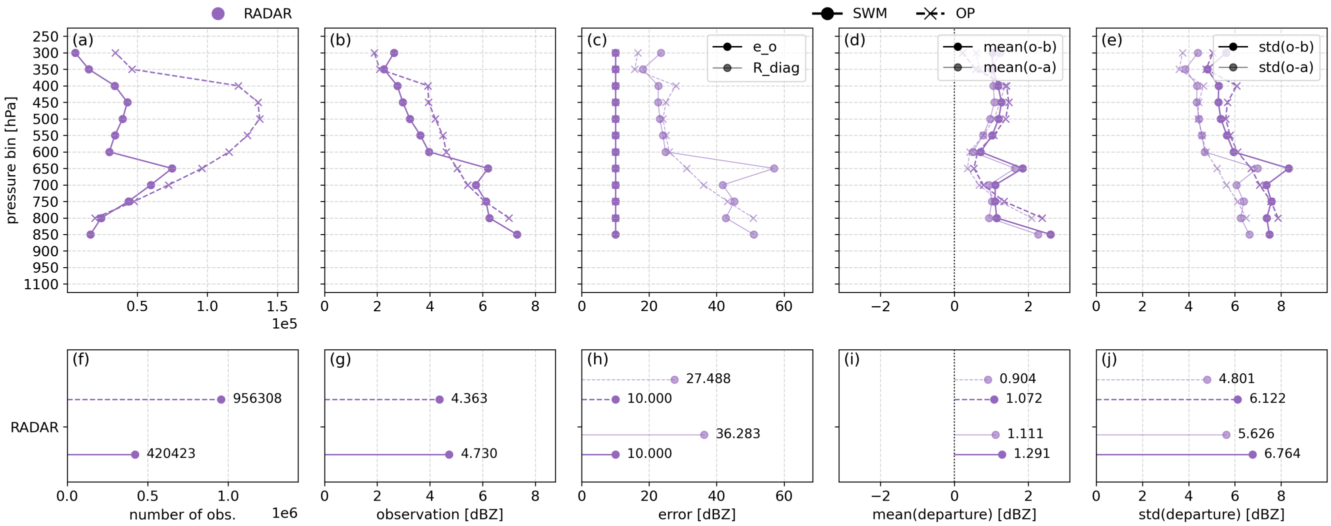

Figure 12. As Fig. 7 but for radar reflectivity ($RADREFL$)

an overall improvement of the modeled RH after assimilation (Fig. 11e,j) and particularly a 22 % improvement from SWM radiosoundings.

4.4 Radar reflectivity

The only OP radar in the BF domain is Deutscher Wetterdienst's C-Band radar located at Feldberg, $30\,\mathrm{km}$ west of Bonndorf, where the SWM X-Band radar was operated. Feldberg lies at $\approx 1500\,\mathrm{m}$ a.s.l. and is the highest point in the southern Black Forest, while Bonndorf lies in the lee of the Black Forest at $\approx 800\,\mathrm{m}$ a.s.l. (Fig. 2b; purple markers). Therefore, the $RADREFL$ values can differ at lower elevation angles, but should be comparable at higher altitudes as the radar volumes partially overlap. Indeed, the averaged vertical profiles of $RADREFL$ of the OP C-band and SWM X-band radar are similar, and, as expected, both show a decrease in $RADREFL$ towards higher altitudes (Fig. 12b).

The number of observations of the SWM X-Band radar is smaller than the number of observations from the OP C-Band radar (Fig. 12a,f) because the SWM radar was only operating from 11 July 2023 and the X-band radar scans a smaller volume than the C-Band radar. The observation error for observation type RADAR is set to $\epsilon_o = 10\,\mathrm{dBz}$ while the error estimate R_{diag} is roughly three times larger for both instruments (Fig. 12c).

Both radars show positive mean departures at all levels (Fig. 12d,j) indicating that the model underestimates the observed reflectivities. This underestimation is reduced by assimilation such that the mean analysis departures are slightly smaller. Furthermore, assimilation reduces the random model error by about 20 % (Fig. 12j) for both OP and SWM observations. The vertical profiles of std($\mathbf{o} - \mathbf{b}$) (Fig. 12e) are very similar for SWM and OP, which underlines the good agreement between the observations from Feldberg and Bonndorf.

https://doi.org/10.5194/essd-2026-352
Preprint. Discussion started: 11 September 2026

4.5 Zenith path delay

The standard deviation of the ZPD background departure std$(\mathbf{o}-\mathbf{b}) = 0.0108$ m is reduced to std$(\mathbf{o}-\mathbf{a}) = 0.0085$ m after assimilation, yielding a $21\,\%$ improvement.

https://doi.org/10.5194/essd-2026-352
Preprint. Discussion started: 11 September 2026

5 Model space evaluation

In this section, we examine the influence of the additionally assimilated observations on the 3D model state by comparing the mean absolute differences between CMPG and CTRL. We shall consider the horizontal wind components, U and V, temperature, T, water vapor mixing ratio, QV, and wind speed WS.

5.1 Reanalysis wind fields

The 3-month average wind speed at 1.5 km altitude in both CMPG and CTRL increases from the Alps towards the North Sea (Fig. 13a; shading) and with height (Fig. 13b; shading). The dominant flow direction during the 3 months is southwesterly (Fig. 13a; black arrows). The vertical cross section (Fig. 13b,d,f,h) cuts from west to east through the BF domain, and thus, through the region where the SMW observations have the largest influence. The main crests of the Black Forest and Vosges mountain ranges modulate the wind speed, leading to enhanced wind speed over the crests and reduced wind speed over the Upper Rhine valley.

The wind speed increment at each time step is calculated as the difference between analysis wind speed and background wind speed. The 3-month mean absolute analysis increment in CMPG is, as expected, largest in the BF domain where most additional observations are assimilated (Fig. 13c; shading). The magnitude of the mean absolute wind speed increment decreases radially away from the measurement sites and its shape fits well to the area where the DWL wind observations are localized (Fig. 3; blue shading). Large wind speed increment values reach up to $5\,\mathrm{km}$ altitude (Fig. 13d; shading), consistent with the vertical localization prescribed in KENDA. The influence of the SWM wind observations is largest between the Rhine valley and the Black Forest mountain peaks and its maximum value is $0.75\,\mathrm{m\,s^{-1}}$. This demonstrates a substantial influence of the SWM observations on the analysis. One reason for this large increment is the spatial overlap of the localization areas of the 12 DWLs (see Fig. 3), i.e., locally the increments of individual observations add up resulting in a large total increment in the BF domain. It can therefore be expected that a reduced vertical and horizontal localization length would reduce the maximum influence of the observations on the analysis. Moreover the mean wind speed increment direction points predominantly westwards (Fig. 13c, black arrows). Thus, CMPG shows weaker mean westerlies than CTRL over southwestern Germany, suggesting that the SWM observations systematically slow down the zonal wind in the ICON-D2 analysis.

The mean absolute increment difference between CMPG and CTRL (Fig. 13e,f) isolates the influence of the additional SWM observations assimilated in CMPG: the strongest signal remains centered over the BF domain with a similar shape and magnitude as the CMPG mean absolute increments themselves (Fig. 13c,d). Outside the BF domain, the CMPG wind speed increment difference is small but nonzero (Fig. 13e; black arrows), showing that there is still an observation influence in a larger region surrounding the BF domain, as the observation influence propagates outside the BF domain.

This can also be concluded from the mean absolute difference between CMPG and CTRL analysis fields (Fig. 13g,h), resulting from the continuous assimilation-forecast cycling. The accumulation of assimilation impact due to the continuous cycling results in larger magnitudes in the mean absolute analysis difference compared to the mean absolute increment difference (cf. Fig. 13e,f and g,h). This also illustrates that the impact of the assimilation is maintained in the short-term forecast. Similarly

https://doi.org/10.5194/essd-2026-352
Preprint. Discussion started: 11 September 2026

Open Access Earth System Science Data Discussions

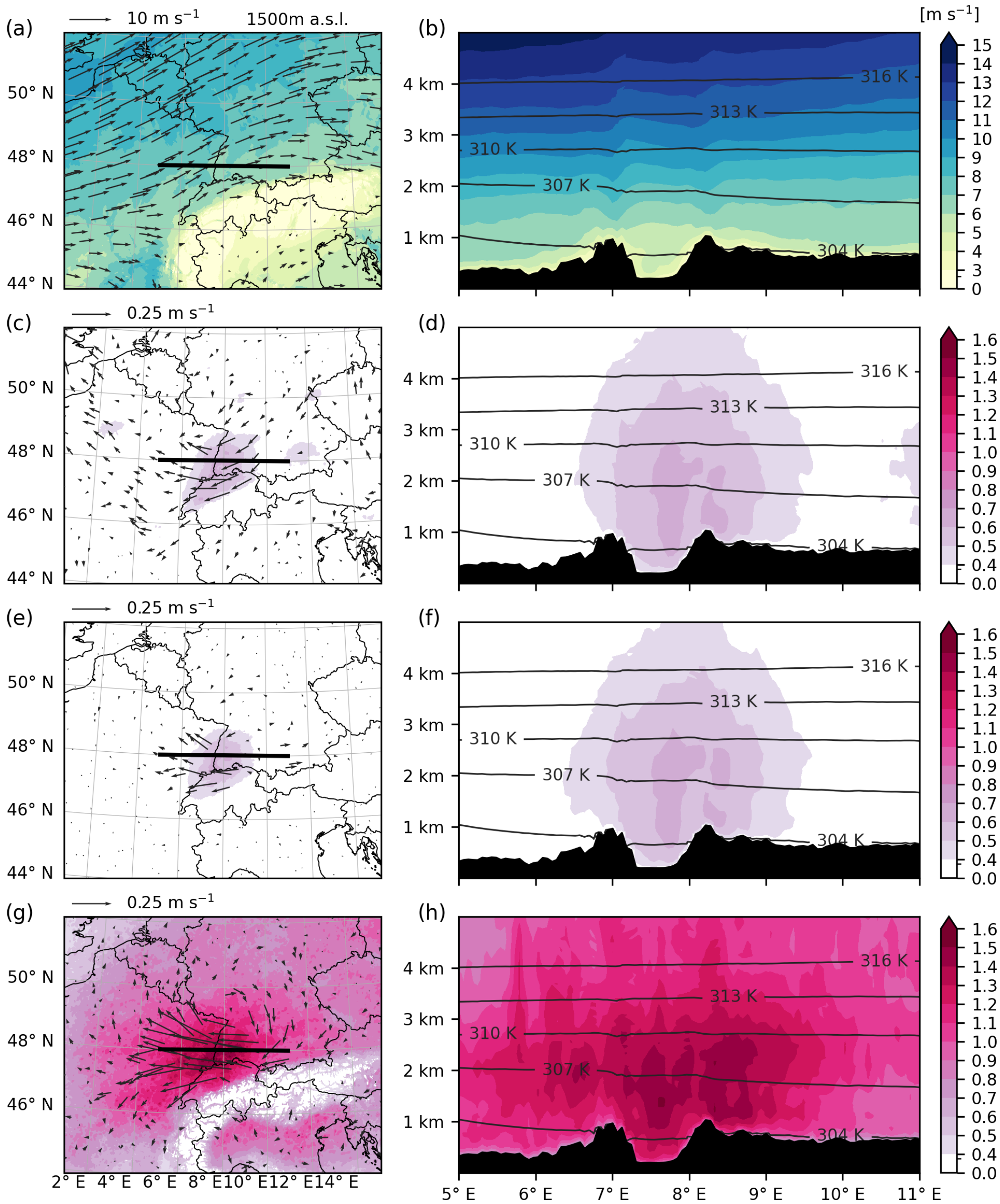

Figure 13. 3-month mean composites averaged over JJA 2023. **(a,c,e,g)**: Horizontal cross section at 1500 m a.s.l.. **(b,d,f,h)**: Vertical cross section crossing the Black Forest at constant latitude (48°N) from 5°E to 11°E (see black line in **a,c,e,g**). The orography (black shading) shows the Vosges mountains at ≈ 7°E, the Upper Rhine valley at ≈ 7.5°E and the Black Forest main crest at ≈ 8.25°E, in the vicinity of which most campaign instruments were located. Black contours indicate levels of constant virtual potential temperature. **(a,b)** mean wind speed (shading) and wind direction (arrows) in CMPG. **(c,d)** mean absolute wind speed increment (shading) and direction of wind increment (arrows) in CMPG. **(e,f)** mean absolute difference (CMPG minus CTRL) of wind speed increment (shading) and direction of the wind increment difference (arrows). **(g,h)** mean absolute difference (CMPG minus CTRL) of analysis wind speed (shading) and direction of the analysis wind difference (arrows).

https://doi.org/10.5194/essd-2026-352
Preprint. Discussion started: 11 September 2026

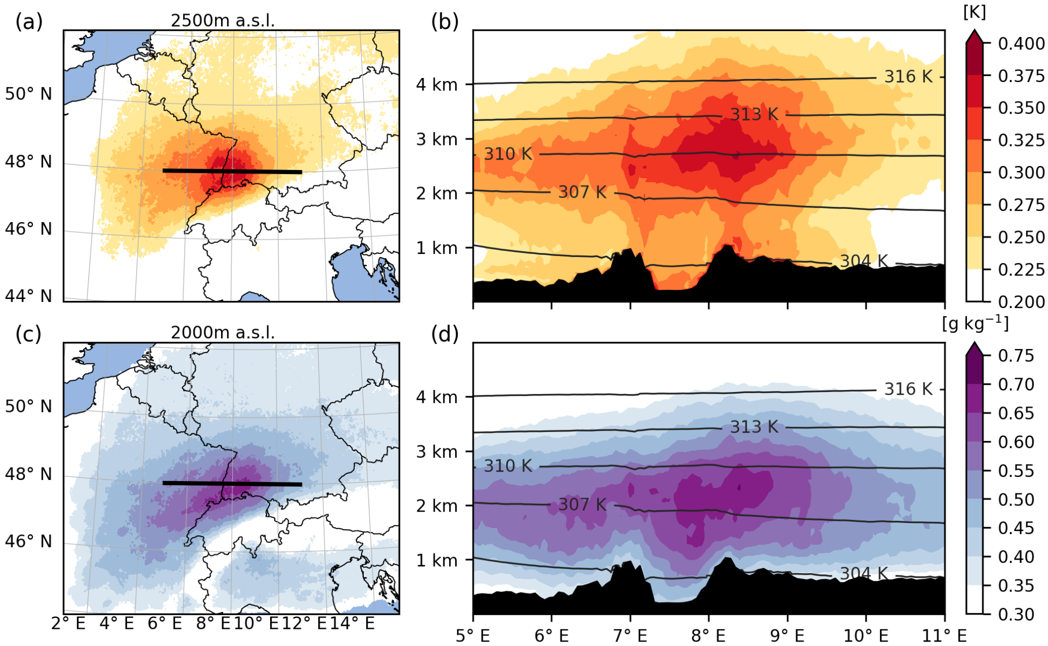

Figure 14. As Fig. 13g,h but for temperature **(a,b)** and for water vapor mixing ratio **(c,d)**.

to the analysis increments, the largest difference in wind fields occurs in the BF domain. In particular, substantial wind speed differences between CMPG and CNTRL reach from 6°E to 9°E. Overall, the maximum absolute wind speed differences are approximately two times larger than the absolute wind speed increment differences in the BF domain (Fig. 13e,f) and an approximately $1\,\mathrm{m\,s^{-1}}$ wind speed difference extends almost over the full ICON-D2 domain. This shows that the influence of the SWM observations is not lost within the 1-hour forecast step, but accumulates over time, as the CMPG wind increments add to an already changed background field. Hence, we conclude that the impact of the wind observations is still present after the forecast step.

5.2 Reanalysis temperature and humidity fields

As for wind speed, the largest mean absolute analysis difference (CMPG – CTRL) in T occurs over the southern Black Forest (Fig. 14a,b). This is consistent with the spatial distribution of additional SWM T observations (radiosondes and SYNOP stations) from within the BF domain as well as with a potential influence of SWM wind measurements on T. However, differences extend well beyond the BF domain, across Germany and into eastern France, but decay consistently with increasing distance, reflecting the effect of horizontal localization and the limited number of additional T observations. In the vertical, the mean absolute T difference peaks at around $2.5\,\mathrm{km}$ a.s.l. and reaches values of up to $0.4\,\mathrm{K}$. This difference is about twice as large than the maximum of the mean absolute T increment in each dataset individually (both CMPG and CTRL) at the same altitude. Similar to the observation impact on the analysis wind field (Section 5.1), the continuous cycling accumulates

https://doi.org/10.5194/essd-2026-352
Preprint. Discussion started: 11 September 2026

the effect of observations and results in a larger difference between CMPG and CTRL analysis compared to the difference between CMPG and CTRL increments.

In the case of water vapor mixing ratio QV, the absolute CMPG – CTRL analysis difference also maximizes over the BF domain (Fig. 14c,d), but the spatial reach is broader than for T. However, the observation influence from assimilating additional ZPD observations was expected to extend over the whole domain which is not visible in the model space cross sections. Therefore, it is unlikely that ZPD observations from GNSS have a substantial influence on the CMPG analysis. The mean absolute CMPG - CTRL difference outside the BF domain has, as in case of the T fields, roughly half the magnitude in the BF domain. It extends farther southwest than in the case of T and there is a difference present even in northern Italy. The vertical extent of the mean absolute CMPG - CTRL difference is also broader for QV than for T and maximizes at $2.5\,\mathrm{km}$ a.s.l. with a value of $0.7\,\mathrm{g\,kg^{-1}}$. The differences in QV between CMPG and CTRL analysis fields can result either directly from assimilating additional RH observations from the SWM radiosondes and $RADREFL$ observations from the SWM X-Band radar or be introduced by covariances between the thermodynamic and dynamic variables.

https://doi.org/10.5194/essd-2026-352
Preprint. Discussion started: 11 September 2026

6 Discussion and outlook

A pioneering, convection-permitting campaign reanalysis is presented that incorporates an unprecedented variety of high-resolution observations from the Swabian MOSES 2023 campaign conducted in southwest Germany during JJA 2023. The campaign reanalysis is created using Deutscher Wetterdienst's ensemble data assimilation framework KENDA, relying on the LETKF, and is computed on the ICON-D2 grid with $2\,\mathrm{km}$ mesh size centered on Germany. The campaign reanalysis (CMPG) uses an identical setup as a control (CTRL) reanalysis, but assimilates operational and campaign observations (OP + SWM), whereby the latter are not assimilated operationally at Deutscher Wetterdienst. SWM observations are (i) wind profiles from 12 Doppler wind lidars (DWLs), (ii) X-band radar reflectivities, (iii) additional radiosoundings, (iv) surface meteorological mast data, and (v) a domain-wide network of GNSS retrieved zenith path delays. Thanks to this rich set of observations, the CMPG reanalysis offers an optimal four-dimensional estimate of the lower-tropospheric state on the regional level. To our knowledge, previous campaign reanalyses have assimilated either (i) fewer additional observation types, (ii) a shorter period, (iii) observations mostly in flat terrain, (iv) not at convection-permitting scale and, most importantly, (v) a lower density of high-resolution atmospheric profile observations. Taken together, these features contribute to the unique, comprehensive, and unprecedented character of the Swabian MOSES 2023 reanalysis dataset (see Fig. 1). Beyond its immediate value for process understanding and model evaluation, this dataset can serve as initial and lateral boundary conditions for targeted predictability studies and nested, higher-resolution model simulations.

In the Black Forest domain (BF domain; Fig. 2), twice as many wind observations are assimilated in the campaign reanalysis (CMPG) than in the control reanalysis (CTRL), which assimilates exclusively operationally available observations (OP). To our knowledge, CMPG is thus the first reanalysis that incorporates wind observations from such a dense network of DWLs. The largest number of Doppler wind lidar (DWL) observations is retrieved and assimilated between $900\,\mathrm{hPa}$ and $600\,\mathrm{hPa}$, addressing a long-recognized observational gap in lower tropospheric dynamics (Bell et al., 2020; Cimini et al., 2020). Locally, the assimilation of campaign observations reduces the systematic model error, $\overline{(\mathbf{o}-\mathbf{a})} < \overline{(\mathbf{o}-\mathbf{b})}$, for all variables assimilated from the campaign. In particular, the improvement in the standard deviation of the departures amounts to $34\,\%$ for DWL retrieved zonal and meridional winds, $26\,\%$ for temperature and $22\,\%$ for relative humidity from SWM radiosoundings, $17\,\%$ for the SWM X-band radar reflectivities, and $21\,\%$ for the GNSS ZPD observations (see Section 4). These values are of the same order of magnitude as the relative improvements by OP observations. Model space evaluation reveals that assimilating SWM observations systematically modifies the state of the troposphere up to $5\,\mathrm{km}$. The SWM observation influence is not confined to the direct vicinity of the observations but influences the lower troposphere over the whole domain through multivariate covariances, continuous cycling, and advection. The mean absolute differences between CMPG and CTRL reach domain-wide magnitudes of order $1\,\mathrm{m\,s^{-1}}$ for wind speed, $0.25\,\mathrm{K}$ for T, and $0.4\,\mathrm{g\,kg^{-1}}$ for QV (see Section 5), and are even larger in the campaign region, with mean absolute differences of $1.5\,\mathrm{m\,s^{-1}}$ in wind speed, $0.4\,\mathrm{K}$ in T, and $0.7\,\mathrm{g\,kg^{-1}}$ in QV. T differences are spatially more confined than QV differences, and reach largest values at higher altitudes. This dataset demonstrates that heterogeneous campaign observations can be assimilated in a quasi-operational setup over complex terrain to yield an exten-

https://doi.org/10.5194/essd-2026-352
Preprint. Discussion started: 11 September 2026

sive, convective-scale reanalysis that statistically reduces the difference between model and observations for all assimilated variables, thereby reshaping the representation of the dynamics and thermodynamics in the lower troposphere.

At the same time, complex terrain and limited model resolution set key challenges: At $2\,\mathrm{km}$ mesh size, orographic trigger mechanisms of convection are only partially resolved, and local observations may not be representative for resolved model fields. While observation-to-background differences for the campaign observations included in this reanalysis indicate no systematic problem with representativity, previous studies have shown that even $1\,\mathrm{km}$ analyses can overestimate nighttime ground temperatures in narrow valleys (Bugnard et al., 2025) and miss flow variability in complex terrain (Goger and Dipankar, 2024), emphasizing the need for yet finer grids and denser lower-tropospheric profiling. Efforts are currently being made to establish on-demand setups for assimilation and forecasting in complex terrain at even higher resolution, such as the Global-to-Regional ICON Alpine Twin (GLORI-A) with $500\,\mathrm{m}$ mesh size. Moreover, adding many observations within a small domain poses new challenges, such as determining appropriate observation thinning procedures and appropriately weighting different observation types from the same location. This is particularly relevant when their departures have opposite signs, as found in DWL and RWP observations used in the CMPG reanalysis. Novel data assimilation approaches are being designed to better exploit a denser observational content, by leveraging the underlying model dynamical core (Pasmans et al., 2024). The mean and standard deviation of the CMPG observation space departures are in agreement with those of previous campaign reanalyses (Keil and Cardinali, 2004; Fourrié et al., 2019). However, the reduction of the departures by data assimilation, i.e., the difference between $\overline{(\mathbf{o}-\mathbf{b})}$ and $\overline{(\mathbf{o}-\mathbf{a})}$ statistics is more pronounced in Fourrié et al. (2019) than it is in this study. Such differences can result from a different data assimilation setup, geographical area, assimilation period, and synoptic condition.

The Swabian MOSES 2023 campaign reanalysis provides manifold research applications, such as an assessment of the influence of additional wind profile observations with a focus on the representation of the mesoscale circulation in the boundary layer over complex terrain or the application of the Partial Analysis Increment diagnostic (PAI; Diefenbach et al., 2023) to disentangle the influence of individual observations on the total analysis increment. The campaign reanalysis, which is consistent with campaign observations, provides a basis for detailed case studies of high-impact convective events and convection initiation, and can be employed as initial and lateral boundary conditions for sub-kilometer resolution simulations. Moreover, the consistent reanalysis datasets provide a valuable basis for various machine-learning applications, such as methods of explainable and causal AI for understanding and predicting convection. Systematic re-forecast experiments initialized from the CMPG and CTRL reanalyses facilitate the quantification of observation impact on forecasts. Overall, these efforts can contribute to the investigation of potential model weaknesses in complex terrain. The developed setup further builds a valuable basis for new and even higher-resolution campaign reanalyses, for example for the alpine TEAMx campaign (Rotach et al., 2022). TEAMx additionally incorporated a network of novel differential absorption lidars for humidity profiling of the ABL. While further sensitivity experiments with respect to localization length scales and observation thinning may be needed for operational NWP, these efforts help to understand how additional profiling of the lower troposphere can improve convective-scale analysis and forecasts in complex terrain.

https://doi.org/10.5194/essd-2026-352
Preprint. Discussion started: 11 September 2026

Open Access Earth System Science Data Discussions

7 Data availability

The deterministic campaign (CMPG) and reference (CTRL) reanalysis datasets as well as postprocessed observations space data will permanently be made publicly available after acceptance of the manuscript in RADAR4KIT. The RADAR4KIT archive is publicly accessible. Each reanalysis dataset has a size of $0.7\,\mathrm{TB}$ and is stored separately for each month. During the review process, the datasets are available from temporary repositories:

- https://radar.kit.edu/radar/en/dataset/07gpanyv7pnvhf67?token=koJBZmmUCzepmBMXVCtw (Thomas et al., 2026a)
- https://radar.kit.edu/radar/en/dataset/r3cbytxm7hgcnxgk?token=YHgykxcvGUWLhYgczatK (Thomas et al., 2026b)
- https://radar.kit.edu/radar/en/dataset/kmpb2g46amkneczs?token=bJHKRzlsGEFLjwMeiRam (Thomas et al., 2026c)
- https://radar.kit.edu/radar/en/dataset/44crb4kb4k0uvqtv?token=kcOcAbZRJtmpjfFOFnen (Thomas et al., 2026d)
- https://radar.kit.edu/radar/en/dataset/4bdfdmsbc37u516u?token=BuEPnqhtAmIaxarauQPy (Thomas et al., 2026e)
- https://radar.kit.edu/radar/en/dataset/g5n6qsnzy27r3m0c?token=vemBLzLymGjqSnHsaidr (Thomas et al., 2026f)
- https://radar.kit.edu/radar/en/dataset/zppude9j5q2naauz?token=aPxEJjCxysScOchSKsZS (Thomas et al., 2026g)

Author contributions. JT performed the data analysis and wrote the original draft of the manuscript. AO, PK, and JK conceptualized the reanalysis and AO acquired funding. AO, HR, TS, and GG designed the assimilation experiments, and HR, TS, and GG conducted the experiments at Deutscher Wetterdienst. AE, PG and MH provided the wind profiles retrieved from the Doppler wind lidars, and AO collected and transferred all campaign observations to Deutscher Wetterdienst. HR, TS, KS, JT, and AO monitored the assimilation cycling and secured the data. JT and AO evaluated the experiments with input from AC and PK. All authors discussed the results and contributed to revising the manuscript.

Competing interests. The authors declare that they have no conflict of interest.

Acknowledgements. This project was carried out within the Italia – Deutschland science-4-services network in weather and climate (IDEA-S4S; INVACODA, 4823IDEAP6). This Italian-German research network of universities, research institutes and Deutscher Wetterdienst is funded by the BMV (Federal Ministry of Transport).

Parts of this work were performed on the computational resource bwUniCluster funded by the Ministry of Science, Research and the Arts Baden-Württemberg and the Universities of the State of Baden-Württemberg, Germany, within the framework program bwHPC. The authors also gratefully acknowledge the computing time provided on the high-performance computer HoreKa by the National High-Performance Computing Center at KIT (NHR@KIT). This center is jointly supported by the Federal Ministry of Education and Research and the Ministry

https://doi.org/10.5194/essd-2026-352
Preprint. Discussion started: 11 September 2026

of Science, Research and the Arts of Baden-Württemberg, as part of the National High-Performance Computing (NHR) joint funding program (https://www.nhr-verein.de/en/our-partners). HoreKa is partly funded by the German Research Foundation (DFG).

The Large Scale Data Facility is funded and supported by the Helmholtz research programme "Supercomputing" of the Helmholtz Association of German Research Centres and of the Ministry for Science, Research and Arts of the state of Baden-Württemberg.

We thank Virginia Poli and Thomas Gastaldo from ARPAE Emiglia-Romagna for their helpful discussions about radar data assimilation and observation monitoring. Moreover, we thank Michael Bender for taking care of the GNSS assimilation. Finally, the authors thankfully acknowledge the support of the Swabian MOSES measurement campaign team in conducting the field measurement campaign. Especially the essential effort of the KITcube team under the coordination of Andreas Wieser is thankfully acknowledged. We kindly acknowledge funding for the field campaign from the Helmholtz Association within the framework of MOSES.

https://doi.org/10.5194/essd-2026-352
Preprint. Discussion started: 11 September 2026

References

Anderson, J. L. and Anderson, S. L.: A Monte Carlo Implementation of the Nonlinear Filtering Problem to Produce Ensemble Assimilations and Forecasts, Monthly Weather Review, 127, 2741–2758, https://doi.org/10.1175/1520-0493(1999)127<2741:AMCIOT>2.0.CO;2, 1999.

Bachmann, K., Keil, C., Craig, G. C., Weissmann, M., and Welzbacher, C. A.: Predictability of Deep Convection in Idealized and Operational Forecasts: Effects of Radar Data Assimilation, Orography, and Synoptic Weather Regime, Monthly Weather Review, 148, 63–81, https://doi.org/10.1175/MWR-D-19-0045.1, 2020.

Baker, W. E., Atlas, R., Cardinali, C., Clement, A., Emmitt, G. D., Gentry, B. M., Hardesty, R. M., Källén, E., Kavaya, M. J., Langland, R., Ma, Z., Masutani, M., McCarty, W., Pierce, R. B., Pu, Z., Riishojgaard, L. P., Ryan, J., Tucker, S., Weissmann, M., and Yoe, J. G.: Lidar-Measured Wind Profiles: The Missing Link in the Global Observing System, Bull. Amer. Meteor. Soc., 95, 543–564, https://doi.org/10.1175/BAMS-D-12-00164.1, 2014.

Baldauf, M., Seifert, A., Förstner, J., Majewski, D., Raschendorfer, M., and Reinhardt, T.: Operational Convective-Scale Numerical Weather Prediction with the COSMO Model: Description and Sensitivities, Monthly Weather Review, 139, 3887–3905, https://doi.org/10.1175/MWR-D-10-05013.1, 2011.

Bechtold, P., Bazile, E., Guichard, F., Mascart, P., and Richard, E.: A mass-flux convection scheme for regional and global models, Quarterly Journal of the Royal Meteorological Society, 127, 869–886, https://doi.org/10.1002/qj.49712757309, 2001.

Bell, T. M., Greene, B. R., Klein, P. M., Carney, M., and Chilson, P. B.: Confronting the boundary layer data gap: evaluating new and existing methodologies of probing the lower atmosphere, Atmospheric Measurement Techniques, 13, 3855–3872, https://doi.org/10.5194/amt-13-3855-2020, 2020.

Bevis, M., Businger, S., Herring, T. A., Rocken, C., Anthes, R. A., and Ware, R. H.: GPS meteorology: Remote sensing of atmospheric water vapor using the global positioning system, Journal of Geophysical Research: Atmospheres, 97, 15 787–15 801, https://doi.org/10.1029/92JD01517, 1992.

Bishop, C. H., Etherton, B. J., and Majumdar, S. J.: Adaptive Sampling with the Ensemble Transform Kalman Filter. Part I: Theoretical Aspects, Monthly Weather Review, 129, 420–436, https://doi.org/10.1175/1520-0493(2001)129<0420:ASWTET>2.0.CO;2, 2001.

Bonavita, M. and Lean, P.: 4D-Var for numerical weather prediction, Weather, 76, 65–66, https://doi.org/10.1002/wea.3862, 2021.

Bonavita, M., Torrisi, L., and Marcucci, F.: The ensemble Kalman filter in an operational regional NWP system: preliminary results with real observations, Quarterly Journal of the Royal Meteorological Society, 134, 1733–1744, https://doi.org/10.1002/qj.313, 2008.

Brousseau, P., Vogt, V., Arbogast, E., Martet, M., Thomas, G., and Berre, L.: The operational 3DEnVar data assimilation scheme for the Météo-France convective scale model AROME-France, https://doi.org/10.5194/egusphere-2025-2642, 2025.

Buehner, M., Caron, J.-F., Lapalme, E., Caya, A., Du, P., Rochon, Y., Skachko, S., Bani Shahabadi, M., Heilliette, S., Deshaies-Jacques, M., Chang, W., and Sitwell, M.: The Modular and Integrated Data Assimilation System at Environment and Climate Change Canada (MIDAS v3.9.1), Geoscientific Model Development, 18, 1–18, https://doi.org/10.5194/gmd-18-1-2025, 2025.

Bugnard, A., Collaud Coen, M., Hervo, M., Leuenberger, D., Arpagaus, M., and Monhart, S.: Comparison of temperature and wind profiles between ground-based remote sensing observations and numerical weather prediction model in complex Alpine topography: the Meiringen campaign, Atmospheric Measurement Techniques, 18, 1039–1061, https://doi.org/10.5194/amt-18-1039-2025, 2025.

Carrassi, A., Bocquet, M., Bertino, L., and Evensen, G.: Data assimilation in the geosciences: An overview of methods, issues, and perspectives, WIREs Climate Change, 9, e535, https://doi.org/10.1002/wcc.535, 2018.

Caumont, O., Cimini, D., Löhnert, U., Alados-Arboledas, L., Bleisch, R., Buffa, F., Ferrario, M. E., Haefele, A., Huet, T., Madonna, F., and Pace, G.: Assimilation of humidity and temperature observations retrieved from ground-based microwave radiometers into a convective-scale NWP model, Quarterly Journal of the Royal Meteorological Society, 142, 2692–2704, https://doi.org/10.1002/qj.2860, 2016.

Chambon, P., Mahfouf, J.-F., Audouin, O., Birman, C., Fourrié, N., Loo, C., Martet, M., Moll, P., Payan, C., Pourret, V., and Raspaud, D.: Global Observing System Experiments within the Météo-France 4D-Var Data Assimilation System, Monthly Weather Review, 151, 127–143, https://doi.org/10.1175/MWR-D-22-0087.1, 2023.

Cimini, D., Haeffelin, M., Kotthaus, S., Löhnert, U., Martinet, P., O'Connor, E., Walden, C., Coen, M. C., and Preissler, J.: Towards the profiling of the atmospheric boundary layer at European scale—introducing the COST Action PROBE, Bulletin of Atmospheric Science and Technology, 1, 23–42, https://doi.org/10.1007/s42865-020-00003-8, 2020.

Clark, P., Roberts, N., Lean, H., Ballard, S. P., and Charlton-Perez, C.: Convection-permitting models: a step-change in rainfall forecasting, Meteorological Applications, 23, 165–181, https://doi.org/10.1002/met.1538, 2016.

Clayton, A. M., Lorenc, A. C., and Barker, D. M.: Operational implementation of a hybrid ensemble/4D-Var global data assimilation system at the Met Office, Quarterly Journal of the Royal Meteorological Society, 139, 1445–1461, https://doi.org/10.1002/qj.2054, 2013.

Coniglio, M. C., Hitchcock, S. M., and Knopfmeier, K. H.: Impact of Assimilating Preconvective Upsonde Observations on Short-Term Forecasts of Convection Observed during MPEX, Monthly Weather Review, 144, 4301–4325, https://doi.org/10.1175/MWR-D-16-0091.1, 2016.

Coniglio, M. C., Romine, G. S., Turner, D. D., and Torn, R. D.: Impacts of Targeted AERI and Doppler Lidar Wind Retrievals on Short-Term Forecasts of the Initiation and Early Evolution of Thunderstorms, Monthly Weather Review, 147, 1149–1170, https://doi.org/10.1175/MWR-D-18-0351.1, 2019.

Courtier, P., Andersson, E., Heckley, W., Vasiljevic, D., Hamrud, M., Hollingsworth, A., Rabier, F., Fisher, M., and Pailleux, J.: The ECMWF implementation of three-dimensional variational assimilation (3D-Var). I: Formulation, Quarterly Journal of the Royal Meteorological Society, 124, 1783–1807, https://doi.org/10.1002/qj.49712455002, 1998.

De Haan, S.: High-resolution wind and temperature observations from aircraft tracked by Mode-S air traffic control radar, Journal of Geophysical Research, 116, D10 111, https://doi.org/10.1029/2010JD015264, 2011.

Desroziers, G., Hello, G., and Thépaut, J.: A 4D-Var re-analysis of FASTEX, Quarterly Journal of the Royal Meteorological Society, 129, 1301–1315, https://doi.org/10.1256/qj.01.182, 2003.

Desroziers, G., Berre, L., Chapnik, B., and Poli, P.: Diagnosis of observation, background and analysis-error statistics in observation space, Quart J Royal Meteoro Soc, 131, 3385–3396, https://doi.org/10.1256/qj.05.108, 2005.

Diefenbach, T., Craig, G., Keil, C., Scheck, L., and Weissmann, M.: Partial analysis increments as diagnostic for LETKF data assimilation systems, Quart J Royal Meteoro Soc, 149, 740–756, https://doi.org/10.1002/qj.4419, 2023.

Durran, D. R. and Weyn, J. A.: Thunderstorms Do Not Get Butterflies, Bulletin of the American Meteorological Society, 97, 237–243, https://doi.org/10.1175/BAMS-D-15-00070.1, 2016.

ECMWF: IFS Documentation CY47R3 - Part II: Data assimilation, https://doi.org/10.21957/T445U8KNA, publisher: ECMWF, 2021.

Erdmann, A. and Gasch, P.: Modular wind profile retrieval software for heterogeneous Doppler lidar measurements (AtmoProKIT v1.1), Geoscientific Model Development, 19, 2497–2529, https://doi.org/10.5194/gmd-19-2497-2026, 2026.

Evensen, G.: Sequential data assimilation with a nonlinear quasi-geostrophic model using Monte Carlo methods to forecast error statistics, Journal of Geophysical Research: Oceans, 99, 10 143–10 162, https://doi.org/10.1029/94JC00572, 1994.

Feldmann, M., Blanc, M., Brennan, K. P., Thurnherr, I., Velasquez, P., Martius, O., and Schär, C.: European supercell thunderstorms—A prevalent current threat and an increasing future hazard, Science Advances, 11, eadx0513, https://doi.org/10.1126/sciadv.adx0513, 2025.

Fluck, E., Kunz, M., Geissbuehler, P., and Ritz, S. P.: Radar-based assessment of hail frequency in Europe, Natural Hazards and Earth System Sciences, 21, 683–701, https://doi.org/10.5194/nhess-21-683-2021, 2021.

Fourrié, N., Nuret, M., Brousseau, P., Caumont, O., Doerenbecher, A., Wattrelot, E., Moll, P., Bénichou, H., Puech, D., Bock, O., Bosser, P., Chazette, P., Flamant, C., Di Girolamo, P., Richard, E., and Saïd, F.: The AROME-WMED reanalyses of the first special observation period of the Hydrological cycle in the Mediterranean experiment (HyMeX), Geoscientific Model Development, 12, 2657–2678, https://doi.org/10.5194/gmd-12-2657-2019, 2019.

Gasch, P., Wieser, A., Lundquist, J. K., and Kalthoff, N.: An LES-based airborne Doppler lidar simulator and its application to wind profiling in inhomogeneous flow conditions, Atmospheric Measurement Techniques, 13, 1609–1631, https://doi.org/10.5194/amt-13-1609-2020, 2020.

Gaspari, G. and Cohn, S. E.: Construction of correlation functions in two and three dimensions, Quarterly Journal of the Royal Meteorological Society, 125, 723–757, https://doi.org/10.1002/qj.49712555417, 1999.

Geerts, B., Raymond, D. J., Grubišić, V., Davis, C. A., Barth, M. C., Detwiler, A., Klein, P. M., Lee, W.-C., Markowski, P. M., Mullendore, G. L., and Moore, J. A.: Recommendations for In Situ and Remote Sensing Capabilities in Atmospheric Convection and Turbulence, Bulletin of the American Meteorological Society, 99, 2463–2470, https://doi.org/10.1175/BAMS-D-17-0310.1, 2018.

Goger, B. and Dipankar, A.: The impact of mesh size, turbulence parameterization, and land-surface-exchange scheme on simulations of the mountain boundary layer in the hectometric range, Quarterly Journal of the Royal Meteorological Society, 150, 3853–3873, https://doi.org/10.1002/qj.4799, 2024.

Goger, B., Rotach, M. W., Gohm, A., Stiperski, I., and Fuhrer, O.: Current challenges for numerical weather prediction in complex terrain: Topography representation and parameterizations, in: 2016 International Conference on High Performance Computing & Simulation (HPCS), pp. 890–894, IEEE, Innsbruck, Austria, ISBN 978-1-5090-2088-1, https://doi.org/10.1109/HPCSim.2016.7568428, 2016.

Grundner, A., Beucler, T., Gentine, P., Iglesias-Suarez, F., Giorgetta, M. A., and Eyring, V.: Deep Learning Based Cloud Cover Parameterization for ICON, Journal of Advances in Modeling Earth Systems, 14, e2021MS002 959, https://doi.org/10.1029/2021MS002959, 2022.

Gustafsson, N., Janjić, T., Schraff, C., Leuenberger, D., Weissmann, M., Reich, H., Brousseau, P., Montmerle, T., Wattrelot, E., Bučánek, A., Mile, M., Hamdi, R., Lindskog, M., Barkmeijer, J., Dahlbom, M., Macpherson, B., Ballard, S., Inverarity, G., Carley, J., Alexander, C., Dowell, D., Liu, S., Ikuta, Y., and Fujita, T.: Survey of data assimilation methods for convective-scale numerical weather prediction at operational centres, Quarterly Journal of the Royal Meteorological Society, 144, 1218–1256, https://doi.org/10.1002/qj.3179, 2018.

Hacker, J., Draper, C., and Madaus, L.: Challenges and Opportunities for Data Assimilation in Mountainous Environments, Atmosphere, 9, 127, https://doi.org/10.3390/atmos9040127, 2018.

Handwerker, J., Barthlott, C., Bauckholt, M., Belleflamme, A., Böhmländer, A., Borg, E., Dick, G., Dietrich, P., Fichtelmann, B., Geppert, G., Goergen, K., Güntner, A., Hammoudeh, S., Hervo, M., Hühn, E., Kaniyodical Sebastian, M., Keller, J., Kohler, M., Knippertz, P., Kunz, M., Landmark, S., Li, Y., Mohannazadeh, M., Möhler, O., Morsy, M., Najafi, H., Nallasamy, N. D., Oertel, A., Rakovec, O., Reich, H., Reich, M., Saathoff, H., Samaniego, L., Schrön, M., Schütze, C., Steinert, T., Vogel, F., Vorogushyn, S., Weber, U., Wieser, A., and Zhang, H.: From initiation of convective storms to their impact — the Swabian MOSES 2023 campaign in southwestern Germany, Frontiers in Earth Science, 13, 1555 755, https://doi.org/10.3389/feart.2025.1555755, 2025.

https://doi.org/10.5194/essd-2026-352
Preprint. Discussion started: 11 September 2026

Hirt, M., Rasp, S., Blahak, U., and Craig, G. C.: Stochastic Parameterization of Processes Leading to Convective Initiation in Kilometer-Scale Models, Monthly Weather Review, 147, 3917–3934, https://doi.org/10.1175/MWR-D-19-0060.1, 2019.

Hitchcock, S. M., Coniglio, M. C., and Knopfmeier, K. H.: Impact of MPEX Upsonde Observations on Ensemble Analyses and Forecasts of the 31 May 2013 Convective Event over Oklahoma, Monthly Weather Review, 144, 2889–2913, https://doi.org/10.1175/MWR-D-15-0344.1, 2016.

Hoeppe, P.: Trends in weather related disasters – Consequences for insurers and society, Weather and Climate Extremes, 11, 70–79, https://doi.org/10.1016/j.wace.2015.10.002, 2016.

Hogan, R. J. and Bozzo, A.: A Flexible and Efficient Radiation Scheme for the ECMWF Model, Journal of Advances in Modeling Earth Systems, 10, 1990–2008, https://doi.org/10.1029/2018MS001364, 2018.

Hohenegger, C. and Schär, C.: Predictability and Error Growth Dynamics in Cloud-Resolving Models, Journal of the Atmospheric Sciences, 64, 4467–4478, https://doi.org/10.1175/2007JAS2143.1, 2007.

Houtekamer, P. L. and Mitchell, H. L.: Data Assimilation Using an Ensemble Kalman Filter Technique, Monthly Weather Review, 126, 796–811, https://doi.org/10.1175/1520-0493(1998)126<0796:DAUAEK>2.0.CO;2, 1998.

Houtekamer, P. L. and Zhang, F.: Review of the Ensemble Kalman Filter for Atmospheric Data Assimilation, Monthly Weather Review, 144, 4489–4532, https://doi.org/10.1175/MWR-D-15-0440.1, 2016.

Hristova-Veleva, S., Zhang, S. Q., Turk, F. J., Haddad, Z. S., and Sawaya, R. C.: Assimilation of DAWN Doppler wind lidar data during the 2017 Convective Processes Experiment (CPEX): impact on precipitation and flow structure, Atmos. Meas. Tech., 14, 3333–3350, https://doi.org/10.5194/amt-14-3333-2021, 2021.

Hunt, B. R., Kostelich, E. J., and Szunyogh, I.: Efficient data assimilation for spatiotemporal chaos: A local ensemble transform Kalman filter, Physica D: Nonlinear Phenomena, 230, 112–126, https://doi.org/10.1016/j.physd.2006.11.008, 2007.

Janjić, T., Bormann, N., Bocquet, M., Carton, J. A., Cohn, S. E., Dance, S. L., Losa, S. N., Nichols, N. K., Potthast, R., Waller, J. A., and Weston, P.: On the representation error in data assimilation, Quarterly Journal of the Royal Meteorological Society, 144, 1257–1278, https://doi.org/10.1002/qj.3130, 2018.

Kalthoff, N., Adler, B., Wieser, A., Kohler, M., Träumner, K., Handwerker, J., Corsmeier, U., Khodayar, S., Lambert, D., Kopmann, A., Kunka, N., Dick, G., Ramatschi, M., Wickert, J., and Kottmeier, C.: KITcube a mobile observation platform for convection studies deployed during HyMeX, metz, 22, 633–647, https://doi.org/10.1127/0941-2948/2013/0542, 2013.

Kawabata, T., Iwai, H., Seko, H., Shoji, Y., Saito, K., Ishii, S., and Mizutani, K.: Cloud-Resolving 4D-Var Assimilation of Doppler Wind Lidar Data on a Meso-Gamma-Scale Convective System, Monthly Weather Review, 142, 4484–4498, https://doi.org/10.1175/MWR-D-13-00362.1, 2014.

Keane, R. J., Craig, G. C., Keil, C., and Zängl, G.: The Plant–Craig Stochastic Convection Scheme in ICON and Its Scale Adaptivity, Journal of the Atmospheric Sciences, 71, 3404–3415, https://doi.org/10.1175/JAS-D-13-0331.1, 2014.

Keil, C. and Cardinali, C.: The ECMWF reanalysis of the MAP Special Observing Period, Quarterly Journal of the Royal Meteorological Society, 130, 2827–2849, https://doi.org/10.1256/qj.03.89, 2004.

Kober, K. and Craig, G. C.: Physically Based Stochastic Perturbations (PSP) in the Boundary Layer to Represent Uncertainty in Convective Initiation, Journal of the Atmospheric Sciences, 73, 2893–2911, https://doi.org/10.1175/JAS-D-15-0144.1, 2016.

Kunz, M. and Puskeiler, M.: High-resolution assessment of the hail hazard over complex terrain from radar and insurance data, Meteorologische Zeitschrift, 19, 427–439, https://doi.org/10.1127/0941-2948/2010/0452, 2010.

Lange, H. and Janjić, T.: Assimilation of Mode-S EHS Aircraft Observations in COSMO-KENDA, Monthly Weather Review, 144, 1697–1711, https://doi.org/10.1175/MWR-D-15-0112.1, 2016.

Lapillonne, X., Hupp, D., Gessler, F., Walser, A., Pauling, A., Lauber, A., Cumming, B., Osuna, C., Müller, C., Merker, C., Leuenberger, D., Leutwyler, D., Alexeev, D., Vollenweider, G., Van Parys, G., Jucker, J., Jansing, L., Arpagaus, M., Induni, M., Jacob, M., Kraushaar, M., Jähn, M., Stellio, M., Fuhrer, O., Baumann, P., Steiner, P., Kaufmann, P., Dietlicher, R., Müller, R., Kosukhin, S., Schulthess, T. C., Schättler, U., Cherkas, V., and Sawyer, W.: Operational numerical weather prediction with ICON on GPUs (version 2024.10), Geoscientific Model Development, 19, 755–772, https://doi.org/10.5194/gmd-19-755-2026, 2026.

Le Dimet, F.-X. and Talagrand, O.: Variational algorithms for analysis and assimilation of meteorological observations: theoretical aspects, Tellus A: Dynamic Meteorology and Oceanography, 38, 97, https://doi.org/10.3402/tellusa.v38i2.11706, 1986.

Leuenberger, D., Koller, M., Fuhrer, O., and Schär, C.: A Generalization of the SLEVE Vertical Coordinate, Monthly Weather Review, 138, 3683–3689, https://doi.org/10.1175/2010MWR3307.1, 2010.

Leutbecher, M.: Ensemble size: How suboptimal is less than infinity?, Quarterly Journal of the Royal Meteorological Society, 145, 107–128, https://doi.org/10.1002/qj.3387, 2019.

Lin, Y.-L., Farley, R. D., and Orville, H. D.: Bulk Parameterization of the Snow Field in a Cloud Model, Journal of Climate and Applied Meteorology, 22, 1065–1092, https://doi.org/10.1175/1520-0450(1983)022<1065:BPOTSF>2.0.CO;2, 1983.

Lorenc, A. C.: Analysis methods for numerical weather prediction, Quarterly Journal of the Royal Meteorological Society, 112, 1177–1194, https://doi.org/10.1002/qj.49711247414, 1986.

Marquis, J. N., Varble, A. C., Robinson, P., Nelson, T. C., and Friedrich, K.: Low-Level Mesoscale and Cloud-Scale Interactions Promoting Deep Convection Initiation, Monthly Weather Review, 149, 2473–2495, https://doi.org/10.1175/MWR-D-20-0391.1, 2021.

Mohr, S., Tonn, M., Augenstein, M., Sperka, C., Kavil Kambrath, G., and Kunz, M.: A 20-year spatio-temporal analysis of 3D radar-based hail tracks in Germany: trends and regional differences, Frontiers in Environmental Science, 14, 1736 782, https://doi.org/10.3389/fenvs.2026.1736782, 2026.

Müller, W. A., Früh, B., Korn, P., Potthast, R., Baehr, J., Bettems, J.-M., Bölöni, G., Brienen, S., Fröhlich, K., Helmert, J., Jungclaus, J., Köhler, M., Lorenz, S., Schneidereit, A., Schnur, R., Schulz, J.-P., Schlemmer, L., Sgoff, C., Pham, T. V., Pohlmann, H., Vogel, B., Vogel, H., Wirth, R., Zaehle, S., Zängl, G., Stevens, B., and Marotzke, J.: ICON: Toward Vertically Integrated Model Configurations for Numerical Weather Prediction, Climate Predictions, and Projections, Bulletin of the American Meteorological Society, 106, E1017–E1031, https://doi.org/10.1175/BAMS-D-24-0042.1, 2025.

Navon, I. M.: Data Assimilation for Numerical Weather Prediction: A Review, in: Data Assimilation for Atmospheric, Oceanic and Hydrologic Applications, edited by Park, S. K. and Xu, L., pp. 21–65, Springer Berlin Heidelberg, Berlin, Heidelberg, ISBN 978-3-540-71055-4 978-3-540-71056-1, https://doi.org/10.1007/978-3-540-71056-1_2, 2009.

Nomokonova, T., Griewank, P. J., Löhnert, U., Miyoshi, T., Necker, T., and Weissmann, M.: Estimating the benefit of Doppler wind lidars for short-term low-level wind ensemble forecasts, Quart J Royal Meteoro Soc, 149, 192–210, https://doi.org/10.1002/qj.4402, 2023.

Parsons, D. B., Lillo, S. P., Rattray, C. P., Bechtold, P., Rodwell, M. J., and Bruce, C. M.: The Role of Continental Mesoscale Convective Systems in Forecast Busts within Global Weather Prediction Systems, Atmosphere, 10, 681, https://doi.org/10.3390/atmos10110681, 2019.

Pasmans, I., Chen, Y., Carrassi, A., and Jones, C. K. R. T.: Tailoring data assimilation to discontinuous Galerkin models, Quarterly Journal of the Royal Meteorological Society, 150, 2820–2847, https://doi.org/10.1002/qj.4737, 2024.

https://doi.org/10.5194/essd-2026-352
Preprint. Discussion started: 11 September 2026

Puskeiler, M., Kunz, M., and Schmidberger, M.: Hail statistics for Germany derived from single-polarization radar data, Atmospheric Research, 178-179, 459–470, https://doi.org/10.1016/j.atmosres.2016.04.014, 2016.

Rahlves, C., Beyrich, F., and Raasch, S.: Scan strategies for wind profiling with Doppler lidar – an large-eddy simulation (LES)-based evaluation, Atmospheric Measurement Techniques, 15, 2839–2856, https://doi.org/10.5194/amt-15-2839-2022, 2022.

Raschendorfer, M.: The new turbulence parametrization of LM., COSMO Newsletter, pp. 89–97, 2001.

Raupach, T. H., Martius, O., Allen, J. T., Kunz, M., Lasher-Trapp, S., Mohr, S., Rasmussen, K. L., Trapp, R. J., and Zhang, Q.: The effects of climate change on hailstorms, Nature Reviews Earth & Environment, 2, 213–226, https://doi.org/10.1038/s43017-020-00133-9, 2021.

Raynaud, L. and Bouttier, F.: The impact of horizontal resolution and ensemble size for convective-scale probabilistic forecasts, Quarterly Journal of the Royal Meteorological Society, 143, 3037–3047, https://doi.org/10.1002/qj.3159, 2017.

Reinert, D., Prill, F., and Frank, H.: DWD Database Reference for the Global and Regional ICON and ICON-EPS Forecasting System, https://www.dwd.de/SharedDocs/downloads/DE/modelldokumentationen/nwv/icon/icon_dbbeschr_aktuell.html, 2025.

Richardson, D. S.: Skill and relative economic value of the ECMWF ensemble prediction system, Quarterly Journal of the Royal Meteorological Society, 126, 649–667, https://doi.org/10.1002/qj.49712656313, 2000.

Robey, R. and Lundquist, J. K.: Behavior and mechanisms of Doppler wind lidar error in varying stability regimes, Atmospheric Measurement Techniques, 15, 4585–4622, https://doi.org/10.5194/amt-15-4585-2022, 2022.

Romine, G. S., Schwartz, C. S., Torn, R. D., and Weisman, M. L.: Impact of Assimilating Dropsonde Observations from MPEX on Ensemble Forecasts of Severe Weather Events, Monthly Weather Review, 144, 3799–3823, https://doi.org/10.1175/MWR-D-15-0407.1, 2016.

Rotach, M. W., Serafin, S., Ward, H. C., Arpagaus, M., Colfescu, I., Cuxart, J., De Wekker, S. F. J., Grubišic, V., Kalthoff, N., Karl, T., Kirshbaum, D. J., Lehner, M., Mobbs, S., Paci, A., Palazzi, E., Bailey, A., Schmidli, J., Wittmann, C., Wohlfahrt, G., and Zardi, D.: A Collaborative Effort to Better Understand, Measure, and Model Atmospheric Exchange Processes over Mountains, Bulletin of the American Meteorological Society, 103, E1282–E1295, https://doi.org/10.1175/BAMS-D-21-0232.1, 2022.

Sakradzija, M., Seifert, A., and Dipankar, A.: A stochastic scale-aware parameterization of shallow cumulus convection across the convective gray zone, Journal of Advances in Modeling Earth Systems, 8, 786–812, https://doi.org/10.1002/2016MS000634, 2016.

Scheck, L., Weissmann, M., and Bach, L.: Assimilating visible satellite images for convective-scale numerical weather prediction: A case-study, Quart J Royal Meteoro Soc, 146, 3165–3186, https://doi.org/10.1002/qj.3840, 2020.

Schomburg, A., Schraff, C., and Potthast, R.: A concept for the assimilation of satellite cloud information in an Ensemble Kalman Filter: single-observation experiments, Quarterly Journal of the Royal Meteorological Society, 141, 893–908, https://doi.org/10.1002/qj.2407, 2015.

Schraff, C., Reich, H., Rhodin, A., Schomburg, A., Stephan, K., Periáñez, A., and Potthast, R.: Kilometre-scale ensemble data assimilation for the COSMO model (KENDA), Quart J Royal Meteoro Soc, 142, 1453–1472, https://doi.org/10.1002/qj.2748, 2016.

Schraff, C., Gebhardt, C., Buchhold, M., and Potthast, R.: Einführung des regionalen Ensemble-basierten Datenassimilationssystems KENDA; Nutzung von ICON-EPS in COSMO-DE-EPS, https://www.dwd.de/DE/fachnutzer/forschung_lehre/numerische_wettervorhersage/nwv_aenderungen/_functions/DownloadBox_modellaenderungen/cosmo_de/pdf_2016_2019/pdf_cosmo_de_21_03_2017.pdf;jsessionid=07A9641578B511BF7C8132F05F8A497D.live21064?__blob=publicationFile&v=2, 2017.

Schumacher, R. S. and Rasmussen, K. L.: The formation, character and changing nature of mesoscale convective systems, Nature Reviews Earth & Environment, 1, 300–314, https://doi.org/10.1038/s43017-020-0057-7, 2020.

https://doi.org/10.5194/essd-2026-352
Preprint. Discussion started: 11 September 2026

Serafin, S., Adler, B., Cuxart, J., De Wekker, S., Gohm, A., Grisogono, B., Kalthoff, N., Kirshbaum, D., Rotach, M., Schmidli, J., Stiperski, I., Večenaj, , and Zardi, D.: Exchange Processes in the Atmospheric Boundary Layer Over Mountainous Terrain, Atmosphere, 9, 102, https://doi.org/10.3390/atmos9030102, 2018.

Stauffer, D. R. and Seaman, N. L.: Use of Four-Dimensional Data Assimilation in a Limited-Area Mesoscale Model. Part I: Experiments with Synoptic-Scale Data, Monthly Weather Review, 118, 1250–1277, https://doi.org/10.1175/1520-0493(1990)118<1250:UOFDDA>2.0.CO;2, 1990.

Stephan, K., Klink, S., and Schraff, C.: Assimilation of radar-derived rain rates into the convective-scale model COSMO-DE at DWD, Quarterly Journal of the Royal Meteorological Society, 134, 1315–1326, https://doi.org/10.1002/qj.269, 2008.

Taszarek, M., Allen, J., Púčik, T., Groenemeijer, P., Czernecki, B., Kolendowicz, L., Lagouvardos, K., Kotroni, V., and Schulz, W.: A Climatology of Thunderstorms across Europe from a Synthesis of Multiple Data Sources, Journal of Climate, 32, 1813–1837, https://doi.org/10.1175/JCLI-D-18-0372.1, 2019.

Team, N. P. I. S., Teixeira, J., Piepmeier, J. R., Nehrir, A. R., Ao, C. O., Chen, S. S., Clayson, C. A., Fridlind, A. M., Lebsock, M., McCarty, W., Salmun, H., Santanello, J. A., Turner, D. D., Wang, Z., and Zeng, X.: Toward a Global Planetary Boundary Layer Observing System: The NASA PBL Incubation Study Team Report, Tech. rep., 2021.

Thomas, G., Martinet, P., Brousseau, P., Chambon, P., Georgis, J., Hervo, M., Huet, T., Löhnert, U., Orlandi, E., and Unger, V.: Assimilation of Ground-Based Microwave Radiometer Temperature Observations Into a Convective-Scale NWP Model for Fog Forecast Improvement, Quarterly Journal of the Royal Meteorological Society, 151, e4893, https://doi.org/10.1002/qj.4893, 2025.

Thomas, J., Reich, H., Steinert, T., Geppert, G., Stephan, K., Erdmann, A., Gasch, P., Hervo, M., Keller, J., Carrassi, A., Knippertz, P., and Oertel, A.: Swabian MOSES 2023 reanalysis dataset, part 1: campaign reanalysis (CMPG) for June 2023, https://radar.kit.edu/radar/en/dataset/07gpanyv7pnvhf67?token=koJBZmmUCzepmBMXVCtw, 2026a.

Thomas, J., Reich, H., Steinert, T., Geppert, G., Stephan, K., Erdmann, A., Gasch, P., Hervo, M., Keller, J., Carrassi, A., Knippertz, P., and Oertel, A.: Swabian MOSES 2023 reanalysis dataset, part 2: campaign reanalysis (CMPG) for July 2023, https://radar.kit.edu/radar/en/dataset/r3cbytxm7hgcnxgk?token=YHgykxcvGUWLhYgczatK, 2026b.

Thomas, J., Reich, H., Steinert, T., Geppert, G., Stephan, K., Erdmann, A., Gasch, P., Hervo, M., Keller, J., Carrassi, A., Knippertz, P., and Oertel, A.: Swabian MOSES 2023 reanalysis dataset, part 3: campaign reanalysis (CMPG) for August 2023, https://radar.kit.edu/radar/en/dataset/kmpb2g46amkneczs?token=bJHKRzlsGEFLjwMeiRam, 2026c.

Thomas, J., Reich, H., Steinert, T., Geppert, G., Stephan, K., Erdmann, A., Gasch, P., Hervo, M., Keller, J., Carrassi, A., Knippertz, P., and Oertel, A.: Swabian MOSES 2023 reanalysis dataset, part 4: control reanalysis (CTRL) for June 2023, https://radar.kit.edu/radar/en/dataset/44crb4kb4k0uvqtv?token=kcOcAbZRJtmpjfFOFnen, 2026d.

Thomas, J., Reich, H., Steinert, T., Geppert, G., Stephan, K., Erdmann, A., Gasch, P., Hervo, M., Keller, J., Carrassi, A., Knippertz, P., and Oertel, A.: Swabian MOSES 2023 reanalysis dataset, part 5: control reanalysis (CTRL) for July 2023, https://radar.kit.edu/radar/en/dataset/4bdfdmsbc37u516u?token=BuEPnqhtAmIaxarauQPy, 2026e.

Thomas, J., Reich, H., Steinert, T., Geppert, G., Stephan, K., Erdmann, A., Gasch, P., Hervo, M., Keller, J., Carrassi, A., Knippertz, P., and Oertel, A.: Swabian MOSES 2023 reanalysis dataset, part 6: control reanalysis (CTRL) for August 2023, https://radar.kit.edu/radar/en/dataset/g5n6qsnzy27r3m0c?token=vemBLzLymGjqSnHsaidr, 2026f.

Thomas, J., Reich, H., Steinert, T., Geppert, G., Stephan, K., Erdmann, A., Gasch, P., Hervo, M., Keller, J., Carrassi, A., Knippertz, P., and Oertel, A.: Swabian MOSES 2023 reanalysis dataset, part 7: observation space statistics for JJA 2023, https://radar.kit.edu/radar/en/dataset/zppude9j5q2naauz?token=aPxEJjCxysScOchSKsZS, 2026g.

https://doi.org/10.5194/essd-2026-352
Preprint. Discussion started: 11 September 2026

Thundathil, R., Zus, F., Dick, G., and Wickert, J.: Assimilation of GNSS tropospheric gradients into the Weather Research and Forecasting (WRF) model version 4.4.1, Geoscientific Model Development, 17, 3599–3616, https://doi.org/10.5194/gmd-17-3599-2024, 2024.

Tiedtke, M.: A Comprehensive Mass Flux Scheme for Cumulus Parameterization in Large-Scale Models, Monthly Weather Review, 117, 1779–1800, https://doi.org/10.1175/1520-0493(1989)117<1779:ACMFSF>2.0.CO;2, 1989.

Vural, J., Merker, C., Löffler, M., Leuenberger, D., Schraff, C., Stiller, O., Schomburg, A., Knist, C., Haefele, A., and Hervo, M.: Improving the representation of the atmospheric boundary layer by direct assimilation of ground-based microwave radiometer observations, Quart J Royal Meteoro Soc, 150, 1012–1028, https://doi.org/10.1002/qj.4634, 2024.

Weckwerth, T. M., Bennett, L. J., Jay Miller, L., Van Baelen, J., Di Girolamo, P., Blyth, A. M., and Hertneky, T. J.: An Observational and Modeling Study of the Processes Leading to Deep, Moist Convection in Complex Terrain, Monthly Weather Review, 142, 2687–2708, https://doi.org/10.1175/MWR-D-13-00216.1, 2014.

Weisman, M. L., Trapp, R. J., Romine, G. S., Davis, C., Torn, R., Baldwin, M., Bosart, L., Brown, J., Coniglio, M., Dowell, D., Evans, A. C., Galarneau, T. J., Haggerty, J., Hock, T., Manning, K., Roebber, P., Romashkin, P., Schumacher, R., Schwartz, C. S., Sobash, R., Stensrud, D., and Trier, S. B.: The Mesoscale Predictability Experiment (MPEX), Bulletin of the American Meteorological Society, 96, 2127–2149, https://doi.org/10.1175/BAMS-D-13-00281.1, 2015.

Weyn, J. A. and Durran, D. R.: The Dependence of the Predictability of Mesoscale Convective Systems on the Horizontal Scale and Amplitude of Initial Errors in Idealized Simulations, Journal of the Atmospheric Sciences, 74, 2191–2210, https://doi.org/10.1175/JAS-D-17-0006.1, 2017.

Wilson, J. W. and Schreiber, W. E.: Initiation of Convective Storms at Radar-Observed Boundary-Layer Convergence Lines, Monthly Weather Review, 114, 2516–2536, https://doi.org/10.1175/1520-0493(1986)114<2516:IOCSAR>2.0.CO;2, 1986.

Yano, J.-I., Ziemiański, M. Z., Cullen, M., Termonia, P., Onvlee, J., Bengtsson, L., Carrassi, A., Davy, R., Deluca, A., Gray, S. L., Homar, V., Köhler, M., Krichak, S., Michaelides, S., Phillips, V. T. J., Soares, P. M. M., and Wyszogrodzki, A. A.: Scientific Challenges of Convective-Scale Numerical Weather Prediction, Bulletin of the American Meteorological Society, 99, 699–710, https://doi.org/10.1175/BAMS-D-17-0125.1, 2018.

Zeng, Y., Blahak, U., and Jerger, D.: An efficient modular volume-scanning radar forward operator for NWP models: description and coupling to the COSMO model, Quarterly Journal of the Royal Meteorological Society, 142, 3234–3256, https://doi.org/10.1002/qj.2904, 2016.

Zeng, Y., Janjić, T., De Lozar, A., Blahak, U., Reich, H., Keil, C., and Seifert, A.: Representation of Model Error in Convective-Scale Data Assimilation: Additive Noise, Relaxation Methods, and Combinations, Journal of Advances in Modeling Earth Systems, 10, 2889–2911, https://doi.org/10.1029/2018MS001375, 2018.

Zeng, Y., Khosravian, K., Feng, Y., De Lozar, A., and Blahak, U.: Investigating radar data assimilation for winter cases using ICON-KENDA system, Atmospheric Research, 312, 107 732, https://doi.org/10.1016/j.atmosres.2024.107732, 2024.

Zhang, F., Snyder, C., and Sun, J.: Impacts of Initial Estimate and Observation Availability on Convective-Scale Data Assimilation with an Ensemble Kalman Filter, Monthly Weather Review, 132, 1238–1253, https://doi.org/10.1175/1520-0493(2004)132<1238:IOIEAO>2.0.CO;2, 2004.

Zängl, G., Reinert, D., Rípodas, P., and Baldauf, M.: The ICON (ICOsahedral Non-hydrostatic) modelling framework of DWD and MPI-M: Description of the non-hydrostatic dynamical core, Quarterly Journal of the Royal Meteorological Society, 141, 563–579, https://doi.org/10.1002/qj.2378, 2015.